High Dynamic-Range Lanthanide-Based Biosensors for Live-Cell Imaging and High Throughput Screening

BY

Ha Thi Pham

B.Sc. VNU University of Science, Vietnam, 2014

THESIS

Submitted as partial fulfillment of the requirements

for the degree of Doctor of Philosophy in Chemistry

in the Graduate College of the

University of Illinois at Chicago, 2020

Chicago, Illinois

Defense Committee:

Lawrence W. Miller, Chair and Advisor
Wonhwa Cho
Xiaojing Yang
Ying Hu
Andrei Karginov, Pharmacology

This thesis is dedicated to my husband, Tung, and my son, Phong,

for their love and support.

ACKNOWLEDGEMENTS

I would like to thank many people for helping me during my doctoral work. First of all, I am grateful to work with Dr. Lawrence Miller, who gave me tremendous help and support during my research in his lab. He has been very patient and kind to me during these years. Without his guidance, I would not accomplish this thesis. Also, I would like to thank my dissertation committee members: Dr. Wonhwa Cho, Dr. Xiaojing Yang, Dr. Ying Hu, and Dr. Andrei Karginov, for their support and letting me use equipment in their lab. I have learned so much when taking Dr. Cho, Dr. Yang, and Dr. Hu's classes.

I would like to thank all staff members in the Department of Chemistry for their support and encouragement. A special thanks to Rhonda, a wonderful person who I will miss a lot. I would like to thank Maggie and Gloria for helping me with the administrative work. I would like to thank Don for helping me fix things at any time.

It was my pleasure working with my labmates in a wonderful lab environment. I am lucky to meet Engin, Xiaoyan, and Megha at the beginning of my Ph.D. and received their support throughout this journey. I am grateful to Ting, Hamid, Claudia, Ali, Yao, and Jesba for their constant support and the great time that we have had together. A special thanks to Mona and Hirushi, who were always there for me and encouraged me when I felt stress.

Last but not least, my deepest gratitude goes to my family. My mom and dad, for their faithful support, love, and encouragement. My sister and brother, Thao and Thang, for standing by my choices. My husband and son, Tung and Phong, for their

unconditional love. They made home a joyful and peaceful place where I restored my energy at the end of the day. Without them, this thesis is not possible.

TABLE OF CONTENTS

Chapter…….Page

I. INTRODUCTION.....1
1.1 Fluorescent Biosensors 2
1.1.1 Cell signaling and its study by fluorescent biosensors.....2
1.1.2 Designing a fluorescent biosensor.....3
1.1.2.1 Choosing the right fluorophores.....4
1.1.2.2 Engineering fluorophores with sensing units 6
1.2 FRET-based Biosensors.....8
1.2.1 Basic Design.....8
1.2.2 Optimization of FRET Biosensors 11
1.2.2.1 The mathematics of FRET efficiency 11
1.2.2.2 Biosensor optimization with distance changes.....13
1.2.2.3 Biosensor optimization with orientation changes 14
1.2.2.4 Biosensor optimization with FRET donor and acceptor pairs 15
1.2.3 Methods of imaging FRET-based biosensors 16
1.2.3.1 Acceptor photobleaching.....16
1.2.3.2 Fluorescence Lifetime Imaging Microscopy (FLIM) 17
1.2.3.3 Sensitized Emission.....18
1.3 Dynamic Range of FRET Biosensors 20
1.3.1 FRET Rac1 biosensors: Exemplary affinity biosensors.....21
1.4 High-throughput Screening 25
1.4.1 Introduction to HTS 25
1.4.2 FRET biosensors as a tool for cell-based HTS 26
1.5 Lanthanide complexes as luminescent probes for imaging and HTS 28
1.5.1 Lanthanide chemistry and photophysics 28
1.5.2 Lanthanide complexes in FRET applications.....32

II. CHARACTERIZING LRET-BIOSENSOR TOOLKIT WITH FKBP12/FRB MODEL.....34
2.1 Introduction.....35
2.2 Materials and Methods.....38
2.2.1 Materials.....38
2.2.2 Methods.....39
2.2.2.1 Cell culture 39
2.2.2.2 Plasmid 39
2.2.2.3 Stable expression of biosensors in mammalian cells 42
2.2.2.4 Probe delivery.....42
2.2.2.5 TGL microscopy and image processing.....43
2.2.2.6 Rapamycin stimulation assay with permeabilized mammalian cells 44

TABLE OF CONTENTS (continued)

Chapter……Page
2.2.2.7 Ascomycin inhibition assay with permeabilized mammalian cells.....45
2.3 Results and Discussion.....45
2.3.1 Biosensor Design.....45
2.3.2 TGL microscopy of biosensors in live cells.....47
2.3.3 Detection of PPIs and their Inhibition in Multi-well plates.....51
2.4 Conclusion.....54
III. RAC1 BIOSENSORS FOR IMAGING AND HTS.....56
3.1 Introduction.....57
3.2 Materials and Methods.....60
3.2.1 Materials.....60
3.2.2 Methods.....61
3.2.2.1 Cell culture.....61
3.2.2.2 Plasmid.....61
3.2.2.3 Biosensor validation - fluorometry assay.....64
3.2.2.4 Multi-well plate assays.....64
3.2.2.5 Stable expression of biosensor plasmids.....66
3.2.2.6 Cell Imaging and Image Processing.....66
3.3 Results and Discussion.....68
3.3.1 Biosensor designs.....68
3.3.2 Biosensor characterization.....70
3.3.3 Biosensors in live cells.....74
3.3.4 Inhibitor assay.....77
3.4 Conclusion.....79
REFERENCES.....81
APPENDIX.....91
VITA.....95

LIST OF FIGURES

Figure……....page

Figure 1. An example of a fluorescence biosensor and its detection of PPIs in live cells. .3

Figure 2. Structure of *A. victoria* GFP.....5

Figure 3. Schematics of dual-chain and single-chain FRET biosensors. 7

Figure 4. Representative FRET-based biosensors for enzyme activities and small molecule analytes. 10

Figure 5. Basic designs of current Rac1 FRET biosensors. 23

Figure 6. Jablonski diagram and emission spectra of a Tb(III) complex. 29

Figure 7. Structure of lanthanide probes. 31

Figure 8. Similarity and differences between FRET and LRET. 33

Figure 9. Set-up of the time-gated luminescence (TGL) detection and schematics of dual-chain and single-chain LRET biosensors of FKBP12/FRB interaction. 37

Figure 10. Chemical structures of Tb probes used in the study. 39

Figure 11. Time-gated luminescence microscopy of the dual-chain FRET biosensor.....48

Figure 12. Time-gated luminescence microscopy of single-chain FRET biosensors. 50

Figure 13. TGL analysis robustly detects FKBP12/FRB interaction and its inhibition following permeabilzation of sensor-expressing cells grown in multiwell plates.....53

Figure 14. Designation of FRET and LRET Rac1 biosensors.. 69

Figure 15. Evaluation of Rac1 biosensors by fluorometry and plate reader assay.....71

Figure 16. Live-cell imaging of Rac1 biosensors.....76

Figure 17. Large reductions were observed in multi-well plate when NSC23766 and EHT 1864 inhibit Rac1 activation.....78

LIST OF ABBREVIATIONS

BRET	Bioluminescence resonance energy transfer
CFP	Cyan fluorescent protein
cpFPs	Circularly permuated fluorescent proteins
eDHFR	Escherichia coli of dihydrofolate reductase
EHT 1864	a Rac1 inhibitor
FKBP12	FK binding protein 12
FLIM	Fluorescence lifetime imaging microscopy
FLM	Fluorescence lifetime measurement
FPs	Fluorescent proteins
FRB	Rapamycin binding domain of m-Tor
FRET	Förster resonance energy transfer
GAPs	GTPase activating proteins
GDIs	Guanine nucleotide dissociation inhibitors
GDP	Guanine diphosphate
GEFs	Guanine nucleotide exchange factors
GFP	Green fluorescent protein
GTP	Guanosine-5'-triphosphate
HTS	High throughput Screening
LRET	Lanthanide-based FRET
NSC23766	a Rac1 inhibitor
PBD	p21-binding domain of Pak1

LIST OF ABBREVIATIONS (continued)

PPIs	Protein-protein interactions
RBD	Rho-binding domain of the effector rhotekin
S/B	Signal-to-background
SBR	Signal-to-background ratio
SW	Signal window
TGL	Time-gated luminescence
TMP	Trimethoprim
TR-FRET	Time-resolved FRET
YFP	Yellow fluorescent protein

SUMMARY

Over the past two decades, considerable efforts have been made to develop tools for elucidating a wide range of biological signaling processes in living cells and animals. Among developed techniques, fluorescent biosensors have proven pivotal for unveiling cellular signaling mechanisms due to the ability to capture the spatiotemporal dynamics of protein-protein interactions (PPIs) in their native environment. The availability of a wide variety of fluorescent proteins, fluorophores, and selective protein labeling methods has genuinely revolutionized the field of biosensor design and optimization. One versatile design format for the construction of genetically encoded biosensors for live-cell imaging is the modulation of Förster resonance energy transfer (FRET) between genetically fused fluorescent proteins (FPs) of different hues. FRET-based biosensors are chimeric proteins that consist of appropriately paired FPs (a donor and an acceptor) linked to one or more polypeptide sensing domains. The sensing domains respond to biochemical changes (e.g., analyte concentration, protein phosphorylation) by changing their conformation or interactions with one another. This, in turn, changes the distance or orientation of the FP FRET pairs, resulting in changes in the FRET signal, which can be observed as a reduction in intensity or lifetime of the donor or an increase in donor-sensitized acceptor emission.

Dynamic range, a key biosensor performance parameter, is defined as the maximum observed difference between the mean, donor-denominated or acceptor-denominated FRET ratios in the On-state and Off-state of the sensor. While popular, many FRET biosensors possess a low dynamic range that barely exceeds the noise of many imaging systems. This limitation mostly comes from the overlapping spectra of

FPs, high non-specific fluorescence in imaging sample, and the large size of FPs which utilize most of the useful FRET distance. Several biosensor templates/toolkits are available to give basic blueprints to achieve a successful biosensor design. However, these toolkits solely focus on optimizing geometrical parameters such as fluorophore distance (using linkers of different length), dipole orientation (using cpFPs), and sensing module domain topology, while the listed limitation sources remain. Furthermore, the existing templates often require empiric testing of many variants to overcome unique structural constraints imposed by each sensing module.

Although widely used in microscopic imaging, FP-based FRET biosensors are less commonly used to detect cellular PPIs at medium throughput or high-throughput applications, especially in cell-based format. This limitation mainly comes from the low dynamic range of FRET biosensors, the relatively small amounts of protein in each sample well, and the fluorescence interference from library compounds. HTS can be designed to run in cell-free or cell-based formats, depending on the availability of resources. In some cases, proteins either cannot be purified or require appropriate post-translational modifications or the presence of additional cellular components. Consequently, the ability to detect PPIs or their inhibition in mammalian cell culture following cell permeabilization in a multi-well plate format represents a substantial advance. At this point in time, there are several non-FRET, cell-based assays for PPI discovery that have been adapted to a high-throughput rate. However, these available cell-based PPI assays experience some limitations, including low signal-to-noise ratio

(SNR), high rates of false positives/negatives, or protein sequestration at non-physiologic sites.

The main objective of this study is to create a lanthanide-based FRET (LRET) biosensor toolkit that aims to simplify and accelerate the generation of high dynamic range biosensors for live-cell imaging and cell-based multi-well plate analysis of PPIs. The kit incorporates a Tb(III) complex as the energy transfer donor, a GFP as the acceptor, and an alpha-helical linker termed ER/K linker as a middle spacer in single-chain biosensor design. Tb and Tb-to-GFP sensitized emission signals have ms-scale lifetimes that permit the use of time-gated luminescence (TGL) detections in which pulsed light is used to excite the Tb complex and sensitized GFP signals are measured after a brief delay. ER/K linkers maintain the donors and acceptor far apart when the sensor is in the open configuration. The unique features of LRET and the incorporation of ER/K linkers generate biosensors with extraordinary dynamic ranges for imaging. TGL of luminescent lanthanide probes has been long used in HTS because it can overcome many limitations of conventional FRET. Here we also explore the potential of LRET sensors in cell-based medium-to-high throughput screening of small molecule inhibitors for PPIs.

In summary, chapter 1 provides a brief introduction to the field of biosensor design and optimization as well as background on relevant scientific concepts and technologies. In chapter 2, we investigate both dual-chain and single-chain configurations of LRET biosensors. Rapamycin-induced interaction between FKBP12 and FRB is used as a model system to characterize biosensor performance in live-cell imaging and multi-

well plate assay. We discuss the advantages and disadvantages of both biosensor configurations and emphasize strategies to overcome the drawbacks. In chapter 3, we apply the biosensor toolkit to improve the dynamic range of current Rac1 biosensors and to design a cell-based multi-well assay to screen for Rac1 inhibitors. Also, reported Rac1 biosensors are performance benchmark to characterize the incorporation of LRET and ER/K linkers in real-world biosensor design. Taken together, the results presented in chapters 2 and 3 show that LRET biosensors are versatile for interrogating PPIs and their function in live cells.

CHAPTER 1

INTRODUCTION

1.1 Fluorescent Biosensors

1.1.1 Cell signaling and its study by fluorescent biosensors

Cellular signal transduction plays a vital role in the cellular communication network. It determines the responses of a cell at multiple levels, from molecular and cellular to tissue and the whole organism. It governs many pivotal cellular decisions, such as cytoskeletal reorganization, cell cycle checkpoints, and apoptosis. As a result, unraveling cell signaling pathways is critical to understanding physiological and pathological cellular function.[1]

Cell signaling information is transmitted, in part, by cascades of protein-protein interactions (PPIs). These interactions are often discrete and transitory in nature.[2] In addition, PPIs require precise temporal and spatial control to exert their function for signal specificity. In fact, many human diseases result from abnormal PPIs, either through the loss of an essential interaction or through the formation of a protein complex at an inappropriate time or location.[3] At this point in time, there are numerous tools to study PPIs, such as affinity chromatography, coimmunoprecipitation, phage display, and NMR spectroscopy. However, these methods often fail to capture the spatiotemporal dynamics of PPIs in their native environment. Consequently, cell-based methods of study are required to overcome this limitation.

Fluorescent biosensors are commonly used to image PPIs in live cells by transducing biological events into changes in fluorescent intensity, wavelength, or lifetime.[4-6] A typical fluorescent lifetime is nanoseconds, making fluorescent biosensors capable of capturing fast interaction when combined with suitable imaging modalities. The emitted fluorescent wavelengths are smaller than many cellular structures, providing

a spatially precise tool to elucidate the spatial distribution of PPIs. Together with the advancement of sophisticated and sensitive microscope hardware, fluorescent biosensors can overcome the limitation of other methods to provide nondestructive and noninvasive visualization of cellular signals with high spatiotemporal resolution in living systems.

1.1.2 Designing a fluorescent biosensor

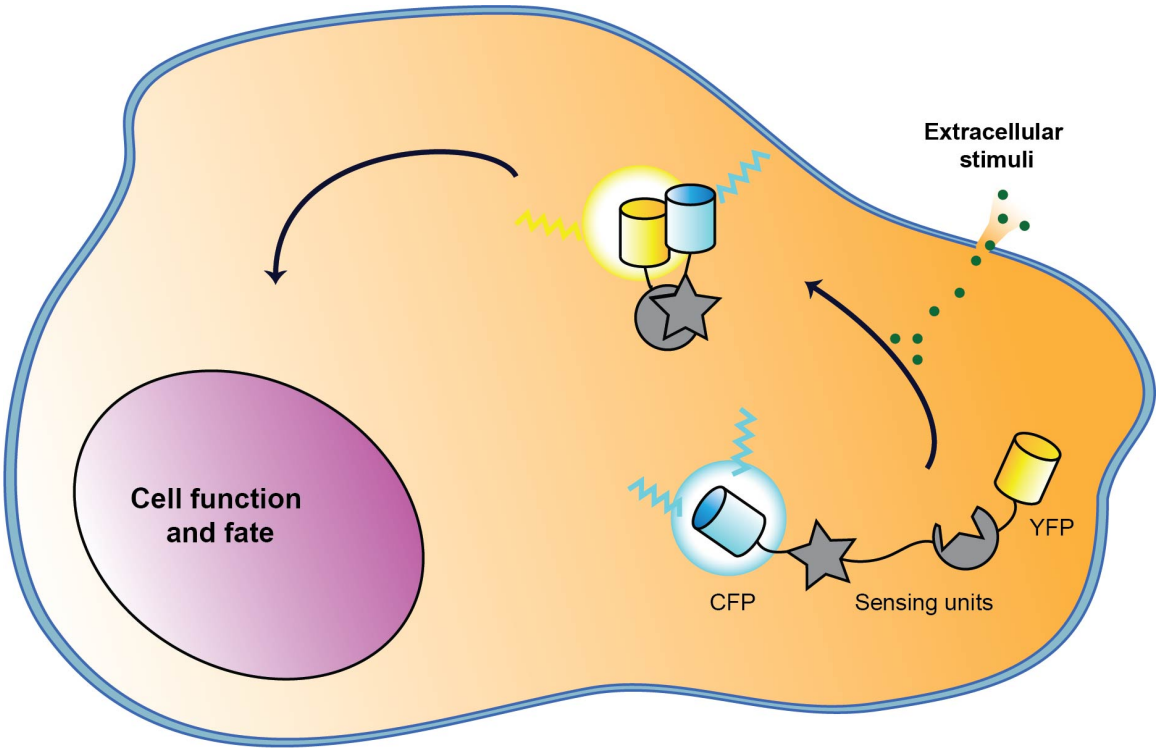

Figure 1. An example of a fluorescence biosensor and its detection of PPIs in live cells. The biosensor consists of sensing units (PPI of interest) and reporting units (cyan and yellow FPs).

Conceptually, a fluorescence biosensor comprises a fluorescent reporting element and a specific signal-sensing element. When target events occur, the molecular state of the signal-sensing element is modified, leading to a quantifiable fluorescent readout of the reporting unit. Usually, the sensing unit is derived from an endogenous cellular protein participating in signal transduction with the target event. For example, the sensing unit of a RhoA biosensor is a Rho-binding domain of the effector rhotekin (RBD), which specifically binds to activated RhoA in RhoA signaling pathway.[7] The reporting unit typically consists of one or more organic dyes or fluorescent protein (FP) variants. The reporting unit is coupled to the sensing unit in a way that change in the target event induces changes in the fluorescent signal (Figure 1). Choosing the right reporting and sensing elements and tinkering them together to maximize fluorescent readout lies at the heart of biosensor design and optimization.

1.1.2.1 Choosing the right fluorophores

The early design of a fluorescent biosensor was limited in scope to proteins that could be purified in vitro and then chemically labeled with organic dyes. These biosensors were then reintroduced into cells via microinjection or electroporation.[8] Organic fluorophores have great properties such as wide spectral range, small size, good photostability, and good brightness. In addition, there are direct or indirect methods to couple fluorophores to the target proteins. However, the greatest problem is controlling the specificity of labeling and defining its stoichiometry. Moreover, purifying the labeled from the unlabeled protein and choosing a suitable method to introduce the sensor into cells make fluorescent biosensors using organic dyes nontrivial to design, optimize and use.[9]

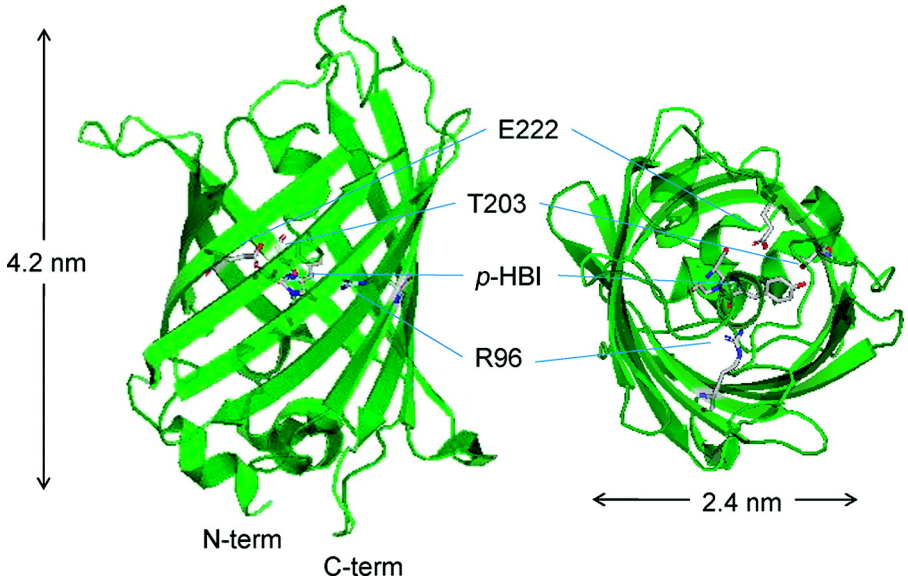

Figure 2. Structure of *A. victoria* GFP. *A. victoria* GFP showing the dimensions of the protein, the intrinsically derived *p*-HBI chromophore and several key residues surrounding the chromophore. Reprinted with permission from Newman, R. H., Fosbrink, M. D., and Zhang, J. (2011) Genetically encodable fluorescent biosensors for tracking signaling dynamics in living cells, *Chem Rev 111*, 3614-3666. Copyright (2011) American Chemical Society.

The discovery of the green fluorescent protein (GFP) from the jellyfish *Aequorea victoria* truly revolutionized the field of fluorescent biosensors for live-cell imaging.[10] Target proteins can be labeled selectively by genetically encoding them as fusions to an FP at the N or C terminus via recombinant cloning. The fused proteins can be expressed intracellularly in selected subsets of cell populations and targeted to specific subcellular microdomains. A growing number of FP-based fluorescent reporters have since been engineered to visualize a wide range of cell activities in living cells.[11-13]

FP engineering plays an important role in optimizing genetically encoded biosensors. Wild-type GFP contains 238 amino acids arranged into 11-stranded β- barrel

with an α-helix and a chromophore located in the middle of the β-barrel structure (Figure 2).[14] Since the GFP chromophore is adequately shielded from external influence, its fluorescence is mostly insensitive to local environmental changes.[10] The earliest available variations of FPs had many limitations in terms of expression, folding, maturation, brightness, excitation/emission spectra, photostability, oligomerization, and environmental sensitivity. However, extensive protein engineering efforts over the last two decades have resulted in improved structural features and a complete spectrum of FP variants, from the near-ultraviolet to the near-infrared, with similarly varying brightness and quantum yield.[15]

1.1.2.2 Engineering fluorophores with sensing units

As mentioned above, the modification of FPs or small organic dyes and their combination with sensing units lies at the heart of biosensor design. Fura-2,[16] a widely-used Ca^{2+} reporter, was an early example of how a fluorescent moiety may be appended to a molecular sensing moiety – in this case, one derived from a Ca^{2+} chelator, EGTA. Upon binding to Ca^{2+}, Fura-2 shifts its excitation peak from 362 nm to 335 nm, providing a quantitative readout of intracellular Ca^{2+} concentrations.

One variation of genetically encoded biosensor may be considered to consist of a single FP that is structurally altered such that it responds to a chemical or physical change in its local environment. In 2005, Magliery et al. reported a method using GFP fragment reassembly to screen for PPIs in bacteria.[17] Briefly, sensing elements were fused to two fragments of GFP split in a loop between residues 157 and 158. Interaction of sensing elements induced GFP assembly, leading to fluorescence. Miesenbock et al. developed pH-sensitive mutants of GFP (pHluorins) to monitor vesicle exocytosis and recycling

through pH inside secretory vesicles.[18] In this design, the engineered GFPs sense pH and report it through a ratiometric fluorescent readout. The fluorescence of circularly permuted FPs (cpFPs) is modulated by conformational switching. A cpFP is generated by fusing its original C and N termini together through a short spacer, while new C and N termini are introduced at specific sites.[19] The fluorescence of FPs depends on the protonation state of its chromophore. The newly-created termini of cpFPs can make the chromophore more accessible to protonation, thereby modulating fluorescence in response to conformational change such as that induced by analyte binding.[20]

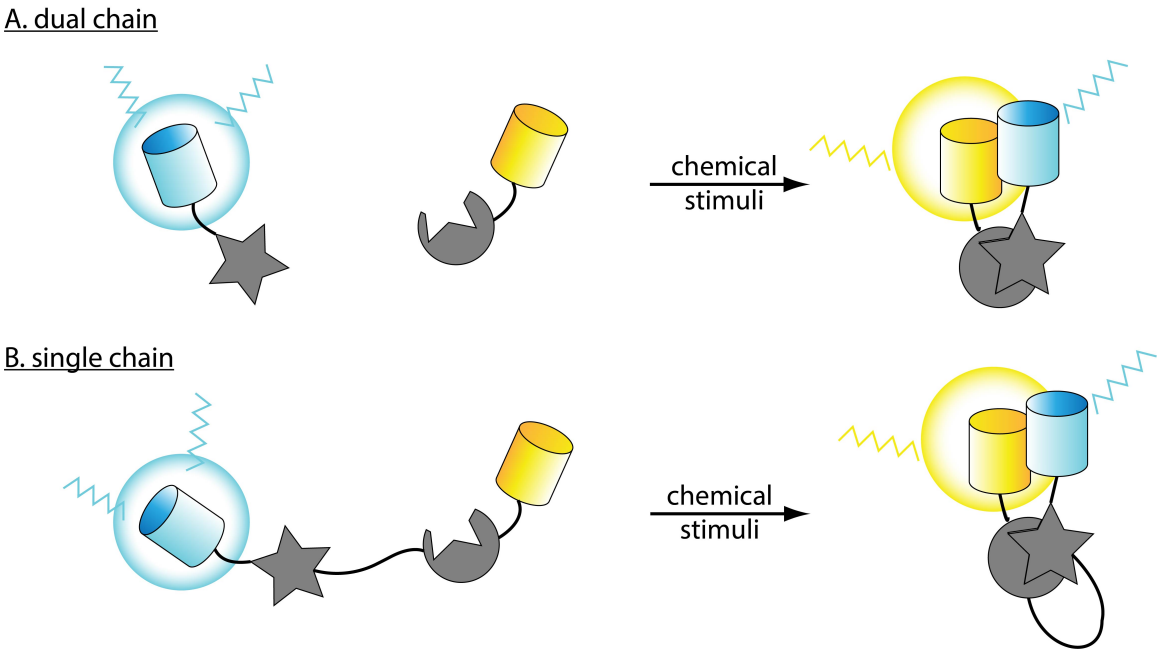

Figure 3. Schematics of dual-chain and single-chain FRET biosensors. (A) In a dual-chain biosensor configuration, sensing units are genetically fused to appropriate FPs. (B) In a single-chain biosensor, sensing units and FPs are fused together as a chimeric protein.

One design that has been proven to be especially versatile for the construction of genetically encoded biosensors is the modulation of Förster resonance energy transfer (FRET) between genetically fused FPs of different hues. FRET is a non-radiative energy transfer between a donor fluorophore and a nearby acceptor fluorophore due to dipole-dipole interaction between the pair. FRET-based biosensors are a critical tool for studying PPIs in live cells. FRET-based biosensors can be achieved with a dual-chain or single-chain configuration. In dual-chain biosensors, sensing units are fused to suitably paired FP donors and acceptors such as cyan and yellow (CFP, YFP) or green and red (GFP, RFP) (Figure 3A). On the other hand, biosensor components are fused together as a chimeric protein in single-chain designs (Figure 3B). In both designs, the sensing domains respond to biochemical changes (e.g., analyte concentration, protein phosphorylation) by changing their conformation or interactions with one another. This, in turn, changes the distance or orientation of the FP FRET pairs, resulting in changes in the FRET signal.

The LRET biosensors generated in this thesis utilize the FRET principle. In the next section, I will discuss in-depth theoretical and practical considerations that must be taken into account when designing, optimizing, and imaging FRET-based biosensors.

1.2 FRET-based Biosensors

1.2.1 Basic Design

FRET is an electrodynamic phenomenon of radiationless energy transfer from a higher-energy donor fluorophore to a lower-energy acceptor chromophore. The energy transfer efficiency or FRET efficiency (E) depends on changes in distance and orientation of the two fluorophores before and after FRET occurs.[6] The donor's characteristic

emission profile will be quenched during FRET, while the acceptor, if fluorescent, will fluoresce with its distinctive emission profile just as though it had been excited directly. A successful biosensor design for studying PPIs in live cells should utilize a mechanism by which specific interaction of target proteins or metabolites can be transduced into a substantial transfer of the donor's internal energy to the acceptor, in other words, significant modulation of FRET efficiency between the pair. Some of the most effective designs are presented in Figure 4.[21]

Most FRET biosensors employ FPs as donors and acceptors due to the robust fluorescence properties of the stable β-barrel structure and the specificity and relative simplicity of genetic encoding. Besides distance and orientation change, photophysical properties of both donor and acceptor, including the quantum yield of donor, extinction coefficient of the acceptor, and spectral overlap between the donor emission and the acceptor absorption affect FRET. Therefore, finding FP pairs that are optimal for FRET was and still remains one of the primary motivations for the continuous engineering and development of FP color variants.

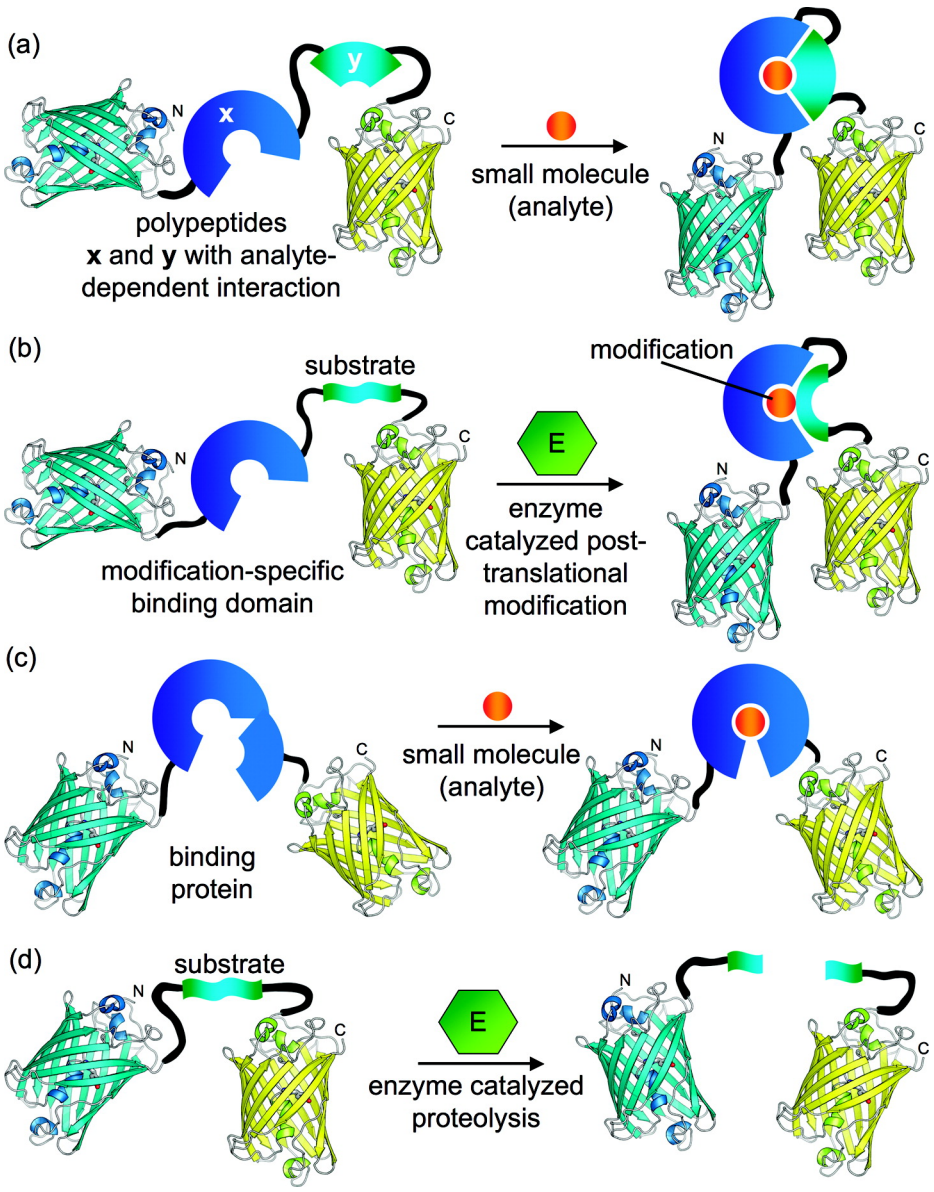

Figure 4. Representative FRET-based biosensors for enzyme activities and small molecule analytes. Although the donor is cyan and the acceptor is yellow in these representations, a variety of other hues could be substituted. (a) Biosensors in which binding of a small molecule induces the association of two distinct moieties within the polypeptide chain.2 (b) Biosensors for posttranslational modification. (c) Biosensors in which a single binding protein undergoes a conformational change upon binding its small molecule ligand. (d) Biosensors for protease activity. Reprinted with permission from Campbell, R. E. (2009) Fluorescent-Protein-Based Biosensors: Modulation of Energy Transfer as a Design Principle, *Anal Chem 81*, 5972-5979. Copyright (2009) American Chemical Society.

1.2.2 Optimization of FRET Biosensors

Biosensor optimization usually takes the most time in biosensor design and often relies on a certain amount of trial and error. In this section, I will highlight optimization strategies that have proven useful in the development of new FRET biosensors. Although logic and intuition can aid in finding of the best design, empirical screening is required. As a result, the following strategies are only starting points for initial designs that must ultimately be evaluated experimentally.

1.2.2.1 The mathematics of FRET efficiency

As noted, FRET is dipole-dipole energy transfer that occurs only when two fluorophores are sufficiently close to one another (less than 10 nm). Therefore, FRET biosensors are designed such that interaction between two affinity domains or conformational switching of a single protein domain alters the distance between the donor and acceptor fluorophores and changes the FRET efficiency. Beside distance, FRET signal changes also can result from changes in the relative ortientation of the fluorophores' dipole moments. These molecular events can be understood further by looking at the mathematics of FRET efficiency (*E*). The Förster theory shows that *E* is described by

$$E = \frac{1}{1 + \frac{r^6}{r_o^6}}$$

where *r* is the interchromophore distance and r_o is the Förster distance (distance where the FRET efficiency is 50 percent, which can be calculated for any pair of fluorescent molecules).[6, 22] According to this equation, E value increases when r decreases. Also, the E value declines sharply around r_o value. Therefore, it is useful to measure FRET within

r_o region where E is more sensitive to r. In theory, FRET should act as a molecular ruler to readout the distance between proteins. However, the signal-to-noise ratio of FRET microscopy is limited such that it is often only possible to differentiate between two states: high FRET or low FRET.

The Förster distance is described by

$$r_o^6 = 8.8 \times 10^{-28} \kappa^2 n^{-4} \Phi_D J$$

where κ^2 is the orientation factor, n is the refractive index, Φ_D is the quantum yield of the donor, and J is the overlap integral between the normalized donor fluorescence and the acceptor excitation spectra. Among these terms, only κ^2 can vary between the on and off states of the biosensor. Thus, we can define constant $C = 8.8 \times 10^{-28} n^{-4} \Phi_D J$ and rewrite E as follow:[21]

$$E = \frac{1}{1 + \frac{r^6}{C\kappa^2}}$$

When a biosensor senses its target event, FRET signal changes, leading to changes in E value (ΔE). The difference of E at the initial and final state of the biosensor is described by the following equation:[21]

$$\Delta E = \left| E_{final} - E_{initial} \right| = \left| \frac{1}{1 + \frac{r_{final}^6}{C\kappa_{final}^2}} - \frac{1}{1 + \frac{r_{initial}^6}{C\kappa_{initial}^2}} \right|$$

According to this equation, $r_{initial}$, $r_{initial}$, $\kappa_{initial}^2$, and κ_{final}^2 are the four variables that directly affect ΔE under typical imaging conditions. These variables represent the distance and orientation of the donor and acceptor fluorophores at the initial and final states of the biosensor. When designing FP-based biosensors, the κ^2 term is

often neglected because it averages to a constant value due to independent motions of each protein domain. A successful FRET biosensor will respond with as large of a signal change as possible upon binding interaction or conformational switching.

1.2.2.2 Biosensor optimization with distance changes

Single-chain biosensors induce FRET through an intramolecular conformational switch. An intuitive strategy for optimizing FRET changes in single-chain configurations, then, is to maximize the change in distance between donor and acceptor by lengthening the middle linker (Figure 3B). However, the polypeptide chain may fold into an Off-state where the FRET partners reside in close proximity regardless of linker length. For example, van Dongen et al. reported a Zn^{2+} biosensor consisting of CFP, Atox1, a flexible peptide as the middle linker, WD4, and YFP. Zn^{2+} induced dimerization of the two metal-binding domains, leading to FRET between CFP and YFP.[21, 23] The authors screened a variety of linkers to optimize biosensor response. However, in contradiction to expectations, increased linker length resulted in smaller FRET efficiency changes in response to Zn^{2+}.

Beside lengthening the middle linker, FRET improvement can be achieved by using dimerizing FPs such as Cypet and Ypet to reduce fluorophore distance in the closed, or high-FRET state.[21] FPs hydrodynamic radii are relatively large (~2 nm) and therefore utilize most of the useful FRET distance. Certain FPs can form a heterodimeric complex at sufficiently high effective molarity, leading to a closer proximity and possibly favored orientations of the fluorophores in the closed state of the biosensor.[24-27] Unlike single-chain biosensors, optimizing FRET is more straightforward for dual-chain and

proteolysis biosensors because each fluorophore is uncoupled in the Off, or low-FRET state.

1.2.2.3 Biosensor optimization with orientation changes

Optimizing FRET biosensors that rely primarily on orientation modulation is challenging as orientation changes are complex and subtle in nature. In general, FRET coupling depends on the orientation angle (κ^2) between the two fluorophores in much the same way as the position of a radio antenna affects its reception. κ^2 adopts a value between 0 and 4 with 0 corresponding to aligned angle (hightest possible E at a given distance) and 4 corresponding to perpendicular angle (minimum E). When integrated over all possible random orientations, κ^2 is assumed to be 2/3.[28] This average value is usually valid for FRET biosensors using unstructured polypeptide linkers, as the linkers are flexible and prevent restriction on spinning and tumbling of the attached fluorophores.

Although one has little control over orientation changes, a few approaches may help adjust κ^2 towards either a particular favorable ($\kappa^2 > 2/3$) or unfavorable ($\kappa^2 < 2/3$) orientation. The first approach is to restrict fluorophore conformation by shortening linkers between the sensing domain and the FP. Second, FPs with both termini internally fused to target proteins likely undergo more conformational restriction.[29] Therefore, instead of N or C-terminal fusion, the donor or acceptor can be inserted into surface-exposed loops of the target. Third, cpFPs are commonly used to vary the critical dipole-dipole orientation. The process of circular permutation involves the fusion of FP natural termini with a peptide linker and introduces new termini in another region. As a result, the cpFP chromophore is exposed to environment and its dipole orientation is sensitive to

conformational switching of the sensing domain. In 2004, Nagai *et al.* reported a successful optimization of a Ca^{2+} biosensor using cpFPs.[30] The biosensor achieved a dynamic range of 560% after optimization. However, one drawback of cpFPs is that their off-state, or low-FRET orientation largely depends on the sensing domain(s) and linker composition. Consequently, it is often necessary to screen many variants in order to identify the biosensor that gives the optimal response.

1.2.2.4 Biosensor optimization with FRET donor and acceptor pairs

The photophysical properties of donor and acceptor fluorophores also affect FRET including the quantum yield of the donor, the extinction coefficient of the acceptor, and the region of overlap between the two spectra. Therefore, to maximize FRET efficiency, one should choose the highest quantum yield donor, the highest absorbing acceptor, and fluorophores with a significant overlap in their spectral profiles. The cyan and yellow colored FP variants, mCerulean and Ypet are among the best FRET pairs for developing genetically encoded biosensors. The FP color palette has been expanded into the orange, red, and far-red regions of the spectrum. However, FPs that emit at longer wavelengths often suffer from long excitation tail that leads to significant crosstalk that obscures the sensitized emission signal.

While popular, FPs have several drawbacks associated with FRET that one should be aware of when designing FP-based FRET biosensors. First, the broad excitation and emission spectra of many FPs results in significant cross-talk. Second, the large size of FPs occupies most of the useful FRET distance, explaining for a 40% reduction of the theoretical FRET efficiency.[31] In addition, the tendency of FPs to dimerize can lead to artifacts when conducting intermolecular FRET experiments.[32] Nonetheless, this

disadvantage can be utilized to increase the FRET signal of biosensors that otherwise exhibit a limited dynamic range. In the later part of the thesis, I will discuss how to overcome FP limitations with lanthanide-to-FP FRET.

1.2.3 Methods of imaging FRET-based biosensors

Upon sensing targeted events, FRET-based biosensors undergo several optical changes that can be detected by various microscope techniques. In the presence of FRET, the donor fluorophore is quenched due to energy transfer to the acceptor, while the acceptor emission intensity, if fluorescent, increases. In addition, the fluorescence lifetime of the donor is inversely proportional to its FRET efficiency. Thus, a direct comparison of the donor lifetime before and after FRET can result in an unambiguous FRET value. The practical challenges when detecting these optical events are to isolate biologically relevant FRET signal changes from other sources of fluorescence present in a live cell. Here, I present three standard methods of imaging FRET-based biosensors: detection of donor dequenching upon acceptor photobleaching, detection of changes in the donor emission lifetime using fluorescence lifetime imaging microscopy, and detection of donor-sensitized acceptor emission at steady state (so-called "filter FRET").[33] Also, the strengths and weaknesses of each method will be emphasized.

1.2.3.1 Acceptor photobleaching

Acceptor photobleaching or donor dequenching FRET can be used to measure the FRET efficiency of a FRET biosensor directly. The underlying concept is that occurrence of FRET leads to a decrease in the donor fluorescence intensity as some of the donor energy is channeled to the acceptor. The amount of decline can be quantified by specifically photobleaching the acceptor (by excitation at its absorption maximum) and

acquiring donor intensity before and after the absence of the acceptor. The efficiency of FRET can be calculated by normalizing the difference between these two intensities to the donor intensity after bleaching. Overall, it is important to ensure the bleaching of the FRET acceptor to ca. 10 percent of its initial value without bleaching the donor.[34]

The primary advantages of using acceptor photobleaching as the fluorescent readout of a fluorescent biosensor are straightforward and quantitative. The FRET efficiency calculated from donor dequenching can be related to PPIs and their spatial distribution. However, this method is destructive and is limited to only a single measurement. As a result, acceptor photobleaching is not suitable to capture PPIs dynamics and precludes time-lapsed studies. Moreover, the photobleaching process can take several minutes or longer, making it hard to capture the transient nature of PPIs. Altogether, the acceptor photobleaching technique limits the advantages of FRET-based biosensors in detecting PPIs, although one may perform the method at the end of an experiment to confirm FRET.

1.2.3.2 Fluorescence Lifetime Imaging Microscopy (FLIM)

FLIM is by far the most accurate method to detect FRET of a fluorescent biosensor. The underlying mechanism of this technique is somewhat related to that of acceptor photobleaching. As FRET occurs, the donor fluorophore of the biosensor becomes quenched by an amount proportional to FRET efficiency. This quenching by FRET leads to a reduction in the fluorescence decay time of the donor. Consequently, FLIM can provide an unambiguous value of FRET efficiency.[35]

The bright side of FLIM is that it can measure FRET independently of changes in biosensor concentration or emission intensity across the sample. Furthermore, FLIM is

not affected by direct acceptor excitation artifacts. The choice of useful FRET pairs is more available because FLIM does not require the acceptor to be fluorescent. On the other hand, there are a number of factors that limit the full use of FLIM in imaging FRET biosensors. The first downside is that FLIM measurements require expensive instrumentation, long (several seconds) image acquisition times, and sophisticated data analysis to resolve nanosecond-scale lifetimes.[35] Additionally, the FLIM approach often requires fluorophores with mono-exponential decays, precluding the use of many FPs.[35, 36] Another drawback is that autofluorescence or changes in environmental factors can shorten the measured fluorescence lifetime as well. Therefore, a great deal of care must be taken into account when analyzing FLIM-FRET data in living cells to eliminate artifacts.

1.2.3.3 Sensitized Emission

Sensitized emission, also referred to as two-color ratio imaging or filter FRET, is by far the most commonly used method to image FRET-based biosensors due to its ease of implementation on wide-field microscopes and reversibility for time-lapse studies. In this method, the biological specimen is illuminated with wavelengths used to excite the donor. Both the donor emission and FRET-sensitized acceptor emission are collected by using corresponding emission filters. As FRET occurs and the two fluorophores are brought closer together in space, the intensity measured through the acceptor filter increases at the expense of the intensity measured through the donor filter. The ratio of acceptor to donor intensity (R) is typically used as a substitute for FRET efficiency in live-cell imaging. For a FRET-based biosensor, the greatest concern in optimization is to obtain maximum changes ($\Delta R = R_{max} - R_{min}$) or, for consistency, percentage changes

($\Delta R/R_{min}$). These values are referred to as the dynamic range of a biosensor that is discussed further in the latter part of the chapter.[21, 36]

Sensitized emission is perhaps the simplest method to quantify the FRET phenomenon. When the dynamic range of FRET biosensors is large, this technique can be beneficial for rapid dynamic experiments due to the ability to acquire both images simultaneously. On the other hand, FRET filter measurement can be hard to measure with precision due to various artifacts. Specifically, when imaging dual-chain biosensors, the method is limited by crosstalk (direct acceptor excitation by the light used to excite the donor), bleedthrough (partial overlap of donor and acceptor emission wavelengths), and nonunitary ratios of donor- and acceptor-labeled proteins. For these reasons, various corrective approaches are required to confirm the presence of FRET. Three images (donor emission, acceptor emission, and FRET-sensitized acceptor emission) must be collected with multiple samples containing: only the donor, only the acceptor, and the FRET sample with both donor and acceptor. The images are then used to subtract the amount of crosstalk, bleedthrough, and fluorescent background from the FRET measurement. Although the true biological FRET signal can be obtained after the correction, it suffers from low signal-to-noise ratio because the error in each measurement is propagated into the final, unmixed FRET image. When it comes to single-chain biosensors, the stoichiometry of the donor and acceptor is a 1:1 ratio. Hence, the image acquisition and processing requirements are less stringent, and two-color, ratiometric imaging is often sufficient to quantify FRET signal changes.[37, 38]

1.3 Dynamic Range of FRET Biosensors

A key biosensor performance parameter is dynamic range. The term "dynamic range" as it applies to FRET biosensors generally refers to the maximum observed difference in the FRET signal between the On state and Off state of the sensor. However, there are subtle distinctions in the way this quantity is measured and reported in the literature. For example, Komatsu *et al.* define dynamic range as the theoretical range of FRET/donor signal ratio between the On state biosensor and that in the Off state.[39] This quantity could be measured either microscopically or spectroscopically by averaging the measured ratios from two cell populations expressing biosensor constructs with appropriate mutations that keep the sensors in the On and Off states. The same authors make a distinction between FRET dynamic range and the "gain" of a biosensor, where gain is the relative increase or decrease in the FRET ratio following stimulation of a sensor-expressing cell population. The gain would be dependent on the biosensor itself, the fraction of the sensor in the On-state under basal conditions, and the amount of stimulant (or inhibitor) added to the cells. In another example, Lam *et al.* define dynamic range as the range of FRET efficiency between the donor and acceptor fluorophores of the sensor.[40] In this study, we define dynamic range as the maximum observed difference in either the mean, donor-denominated or acceptor-denominated FRET ratios (Appendix Table 1).

FP-based FRET biosensors often suffer from low sensitivity in live-cell imaging. As a result, the majority of work in biosensor design is to improve the dynamic range of biosensors. In general, dynamic range should be as large as possible, and its lower boundary is around 30% to isolate FRET from background signal confidently. Dual-chain

and protease biosensors usually exhibit high dynamic range because the donor and acceptor are not intact in one state of the biosensor. On the other hand, single-chain biosensors often suffer from a low dynamic range (lower than 50%) due to high basal FRET of intact fluorophores. Considerable efforts have been made to improve the dynamic range of single-chain FRET biosensors by applying strategies discussed in the previous sections. Here, I would like to analyze the performance of existing Rac1 FRET biosensors as an example of how dynamic range has been optimized over time and its frequent lower and upper boundaries.

1.3.1 FRET Rac1 biosensors: Exemplary affinity biosensors.

Rac1, a member of the Rho family of GTPases, is well recognized for controlling a diverse range of cellular and pathogen process. For about 20 years, rapid progress has been made in understanding Rac1 signaling through the mean of FRET biosensors. Often, the sensing units in Rac1 biosensors are two affinity domains: Rac1 and its downstream effector, the p21-binding domain (PBD) of Pak1. In principle, activated Rac1 (GTP-bound) will bind to PBD, leading to changes in the FRET signal. Dynamic ranges of the following Rac1 biosensors are sampled directly from literature or calculated from reported in vitro fluorescent spectrum analysis. Although it can be an apple-to-orange comparison when experimental conditions are not the same among different studies, one may still obtain a broad picture of dynamic range improvement through this example.

The first Rac1 biosensor, named Rac1 FLAIR, was reported by the Hahn lab in 2000.[41] It was a dual-chain biosensor consisting of Rac1 fused to GFP and PBD labeled by Alexa546 dye (Figure 5A). The former chain was expressed within cells while the latter was microinjected into cells. The corrected Alexa/GFP emission ratio exhibited a

fourfold change upon saturation of Rac1 with GTP (active state), corresponding to a dynamic range of ca. 300%. In 2009, the Hahn lab reported an exclusively genetically encoded version of Rac1 FLAIR in which CyPet and YPet were used as the donor and acceptor (Figure 5B).[42] The dynamic range of this biosensor was not clear from the presented data. Overall, these dual-chain biosensors, while exhibiting high dynamic range, involved cumbersome data analysis because of the non-equimolar distribution of the separated FRET donor–acceptor components. Consequently, researchers have invested time and effort in designing single-chain biosensors.

The first single-chain Rac1 biosensor named Raichu Rac1 was created in the Matsuda lab in 2002.[43] This sensor consists of YFP, PBD, Rac1, CFP, and a CAAX box from N to C terminus with spacers in between each domain (Figure 5C). Spectrometric analysis of the sensor showed a dynamic range of ca. 100%, which was further improved by the incorporation of an EV linker in a later version of the sensor, RaichuEV Rac1.[44] RaichuEV Rac1 exhibited a two-to-threefold rise in FRET when imaging cells expressing the biosensor and stimulated with a growth factor. While possessing a moderate dynamic range and allowing straightforward data analysis, the Raichu sensors disrupt the native interaction of Rac1 with RhoGDI, which is essential to capture faithful spatiotemporal patterns of Rho GTPase activity.

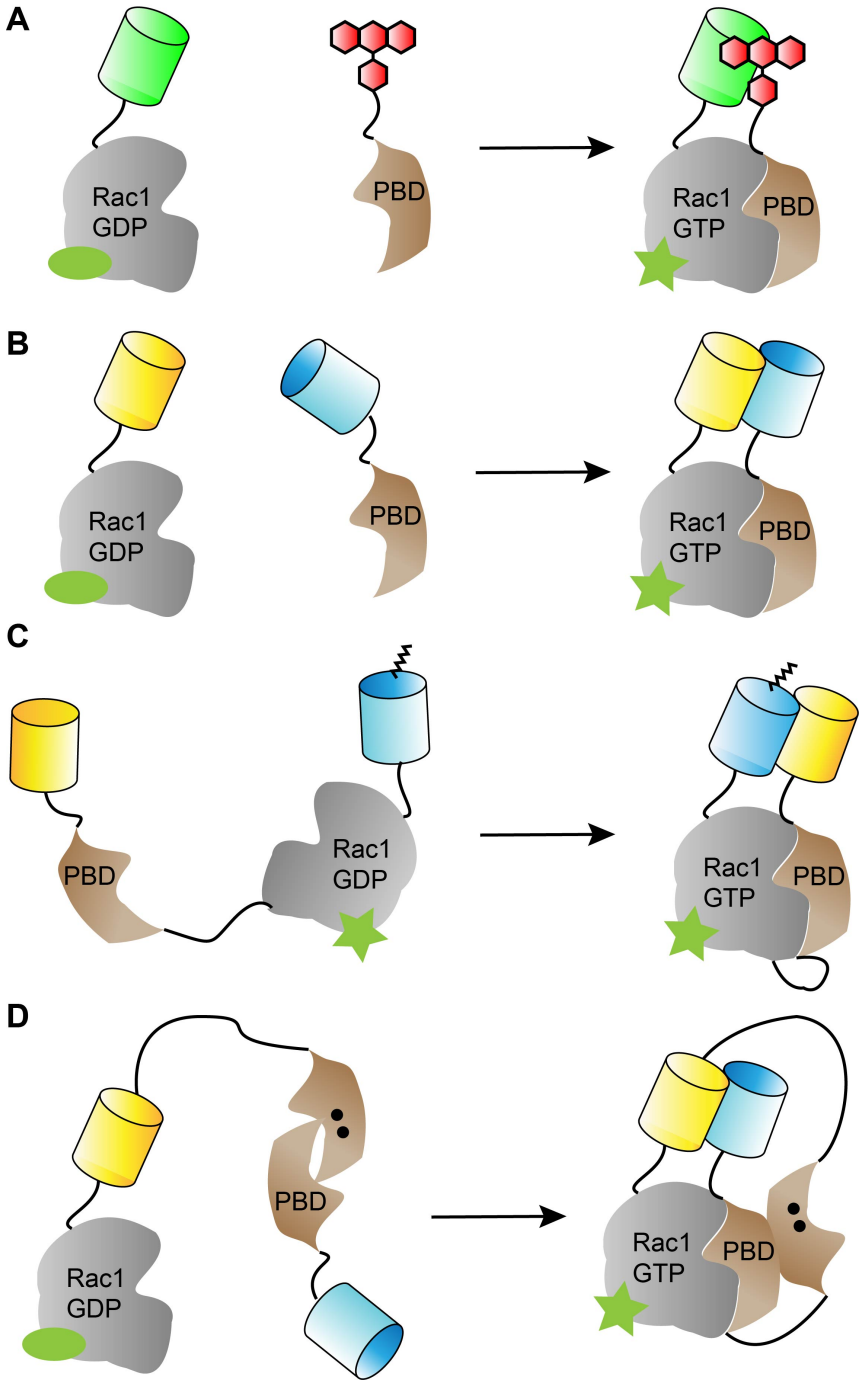

Figure 5. Basic designs of current Rac1 FRET biosensors. Schematic representations of (A) a dual-chain Rac1 FLAIR, (B) an FP-based version of Rac1 FLAIR, (C) a single-chain Raichu Rac1, and (D) a single-chain sensor with Rac1 at C terminus to reserve its interaction with RhoGDI.

In order to retain the interaction of Rac1 with RhoGDI, another class of Rac1 single-chain biosensors was generated with Rac1 being placed at the C terminus of the biosensor. In 2014, the Hodgson lab published a biosensor consisting of mCerulean, two tandem PBDs, separated by a structurally optimized linker, mVenus, and Rac1 (Figure 5D).[45] The sandwiching of the FRET pair between Rac1 and effector domain allows Rac1 at the C terminus; however, it sacrifices the sensor dynamic range (ca. 40%) due to high basal FRET from proximity of the FRET pair. In 2016, the same lab reported an improved version of the biosensor (dynamic range of 146%) by optimizing the dipole coupling of the FRET pair with cpFPs.[46] Similarly, by using the cpFRET toolkit to prepare a biosensor library with built-in geometric diversity, Pertz et al. developed a Rac1-2G biosensor (dynamic range of 69%) able to monitor Rac1 activity in time and space in 2015.[47]

As can be seen from these examples, extensive optimization efforts made over more than a decade were required to obtain current, single-chain FRET Rac1 biosensors that possess a low-to-medium dynamic range. These efforts included selection of optimal FRET partners (e.g., mCerulian/YPet), linker optimization to reduce off-state FRET and leveraging of cpFPs to increase maximal on-state signals. It should also be noted that, despite the wide variety of FPs with different colors and optical properties (e.g., long Stokes-shifts), many sensors, including Rac1, still rely on cyan and yellow FPs. This highlights the difficulties involved not only in developing individual sensors with favorable optical properties, but also in performing multiplexed experiments with two or more FP-sensors in the same cell. In this work, we apply an LRET biosensor toolkit to

overcome the challenges that are evident in current Rac1 sensors as well as other FP-based sensor designs.

1.4 High-throughput Screening

Disruptions or abnormal increases in protein interactions underlie the mechanisms of many diseases. Consequently, drug developers have increasingly focused on searching for small molecules that can disrupt PPIs. However, targeting PPIs with small molecules is nontrivial. The interaction interfaces of proteins are relatively large, while structural information about them is usually unavailable, making rational design of inhibitors largely impossible. Consequently, high-throughput screening (HTS) of thousands of small molecules is required to identify "hit" or "lead" compounds as starting points for further drug development. As discussed earlier, FRET biosensors are a powerful tool to study PPIs due to their spatiotemporal resolution. While commonly used in live-cell imaging, FRET biosensors can also be a promising tool in cell-based HTS applications.

1.4.1 Introduction to HTS

High-throughput screening utilizes robotics, liquid handling devices, and sensitive detectors to scan tens of thousands of compounds daily to identify biologically active molecules. Libraries are stored, and assays are performed in multi-well plates with well densities of 96, 384 or even 1536 wells per plate. In order to quickly scan thousands of molecules with high confidence, HTS assays require substantial signal changes and low variability. Several statistical parameters are used to evaluate HTS assays such as signal window (SW), signal-to-background (S/B), signal-to-noise (S/N) and Z'-factor. SW is a measure of the data range in a high-throughput assay. S/B is the ratio of the positive control mean to the negative control mean. S/N is a similar measure to S/B with the

inclusion of signal variability in the formulation. The Z' factor is a standard quality metric for HTS assays (Appendix Table 1).[48] Z' factor is calculated with the following formula:

$$Z' = 1 - \frac{3(\sigma_p + \sigma_n)}{\mu_p - \mu_n}$$

where, σ_p, σ_n and μ_p, μ_n are the standard deviations and means of the positive and negative control wells, respectively. Z' factor takes into account the assay signal dynamic range and the data variation in the control measurements. *Z'* can vary between -∞ and 1, with values > 0.5 considered to be a very good assay, values between 0 and 0.5 considered marginal, and < 0 an unacceptable assay.[48]

1.4.2 FRET biosensors as a tool for cell-based HTS

HTS can be designed to run in a cell-free, homogenous biochemical environment or cell-based format, depending on the availability of resources. PPIs operate in biologically complex networks and require precise spatiotemporal control to exert specific functions. Thus, live-cell studies are a must in drug discovery, either as early as in HTS or in secondary assays that occur downstream in the process or both. Early in the drug discovery process, homogenous biochemical assays with throughputs of 100,000 of compounds per day are more commonly used than cell-based screens due to cost and the fact that it is challenging to satisfy HTS statistical requirements with a cell-based format. However, incorporating cell-based assays in HTS process can provide three distinct advantages. First, compared to solution-based assays, "hit" compounds found in cell-based assays have a higher chance to be therapeutic agents due to the ability to test for cytotoxicity, membrane permeability, or non-specific interactions. Second, multiple interactions can be screened simultaneously via multiplex assays. Finally, proteins that

cannot be purified or require intracellular modifications can be studied in cell-based screening. As a result, several methods have been reported that permit medium to high throughput screening of PPI inhibition in live cells: methods based on sub-cellular redistribution of fluorescently labeled proteins (suitable for high-content imagers),[49, 50] reporter fragment complementation assays (e.g., split GFP, split luciferase),[51] reporter gene hybrid-like systems,[52, 53] and some methods based on bioluminescence resonance energy transfer (BRET).[39, 54, 55]

Although widely used in microscopic imaging, conventional FP-based FRET biosensors are less commonly used to detect cellular PPIs at medium throughput (96-well plate) or high-throughput (384-well plate), especially in cell-based format.[55] This trend mainly comes from the limitations as mentioned earlier in FRET S/N and dynamic range, the relatively small amounts of protein in each sample well, and the fluorescence interference from library compounds. Consequently, an ideal FRET-based cellular screening platform should present sharp signal changes and low variability. It should adopt optical readout formats that can isolate valid FRET changes from background noise. Fluorescence lifetime measurement (FLM) is an example of such readout formats. FLIM can separate the FRET event from background fluorescent due to its independence of spectra overlap and fluorophore concentration. The recent development of fluorescent lifetime plate readers has increased measurement precision and allows for more robust assay development.[56, 57] Another readout format is time-gated luminescent (TGL) detection of time-resolved FRET (TR-FRET), which is extensively used in HTS campaigns for the discovery of small molecules due to its minimum background interference.[58] In TR-FRET, the fluorescent lifetime of donor fluorophores (luminescent

lanthanide probes) and donor-sensitized FRET are much longer than typical fluorescence. As a result, clean FRET signals can be isolated after a brief delay during which interfering fluorescence background decays. To date, TGL microscopy has been explored for live cell imaging studies[38, 59] and TR-FRET is commonly used in cell-free assays. A biosensor used in both TGL microscopy and cell-based screening is not yet reported.

1.5 Lanthanide complexes as luminescent probes for imaging and HTS

Sensitized complexes of lanthanide cations have unique photophysical properties that make them a powerful fluorescent tool. Particularly, the long emission lifetime, large Stokes shift, and discrete and narrow emission peaks allow temporal and spectral isolation of lanthanide emission signals, making it possible to detect analytes at small concentrations in complex matrices. In fact, lanthanide complexes are routinely employed in diagnostics and high-throughput screening using commercial-plate-reader instrumentation. Recently, there has been increasing interest in applying lanthanide complexes in live-cells microscopic imaging. In this section, I will emphasize the photophysics of lanthanide complexes and its application in imaging and HTS.

1.5.1 Lanthanide chemistry and photophysics

The unique photophysical properties of lanthanides are due to their electronic $[Xe]4f^n$ configuration. First, the shielding by the xenon core makes the valence 4f orbitals 'inner orbitals', leading to minimum perturbation by the surrounding environment.[60] As a result, the emission spectra of lanthanides are very sharp and narrow (<10 nm, half-maximal). Second, because lanthanide f-f transitions are parity-forbidden, direct excitation is inefficient. Consequently, lanthanides have to complex with a sensitizing chromophore, which has a small singlet-triplet energy gap and triplet energy at least 1500

cm^{-1} above the receiving Ln^{3+} level (Figure 6A).[60, 61] The chromophore acts as an antenna to harvest light and transfer to lanthanides for excitation. Furthermore, the forbidden nature slows down the decay of an electron in the excited states to the ground state, resulting in long emission lifetime (from microseconds to milliseconds).[61] Finally, the multiple emission peaks of lanthanides are due to transitions from ^5D orbital to the various ^7F_J ground state orbitals. For example, Tb(III) has four prominent peaks at 490 nm ($^5D_4$ to $^7F_6$), 545 nm ($^5D_4$ to $^7F_5$), 587 nm ($^5D_4$ to $^7F_4$) and 620 nm ($^5D_4$ to $^7F_3$) (Figure 6B).[60]

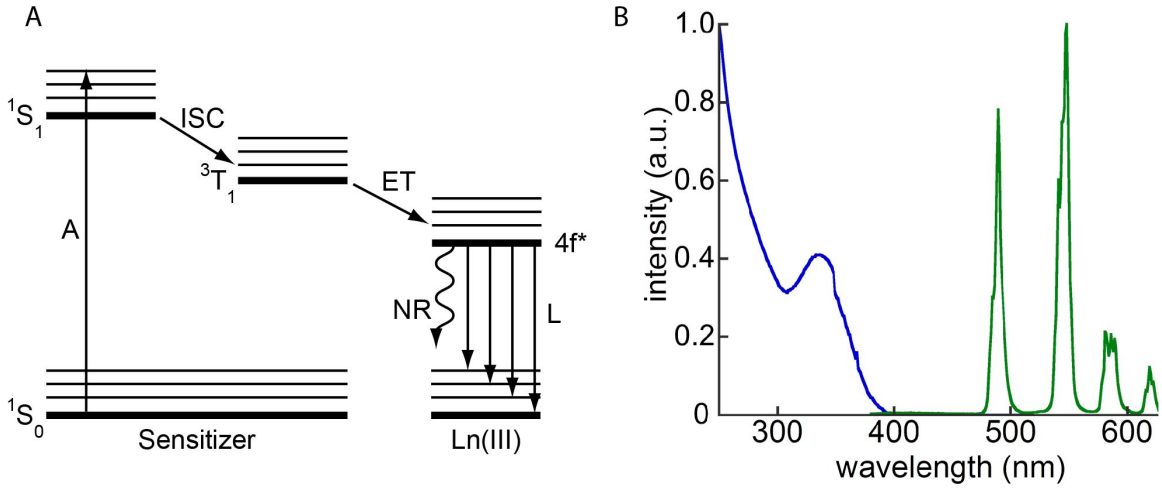

Figure 6. Jablonski diagram and emission spectra of a Tb(III) complex. (A) Jablonski diagram of the energy transfer process for lanthanide complexes. In this diagram, S is singlet state; T is triplet state; A is absorption; L is luminescence; ISC is intersystem crossing; and ET is energy transfer. (B) Excitation (blue) and emission (green) spectra of a terbium complex.

Lanthanide probes consists of a sensitizing chromophore for harvesting light, a chelate to protect lanthanide ions from interactions with the solvent, and a functional group for conjugating to biomolecules (Figure 7A).[60] Complexes of Eu(III) and Tb(III) are the most brightly luminescent lanthanide complexes and most frequently used for luminescence-based sensing. The energy of Eu(III) and Tb(III) optical transitions are such that chromophores with absorption in the near-UV spectral region (300 – 400 nm) are required for sensitization. For biological applications, lanthanide-based probes should have high brightness, structural stability for metal binding, and relatively long-wavelength absorption so as to be compatible with glass optical components and minimally photo-toxic to live cells. For live-cell imaging, the brightness and long excitation wavelength are especially critical because, with millisecond-scale lifetime, lanthanides have a low photon emission rate and cells are sensitive to near UV light. Hundreds of luminescent lanthanide complexes and lanthanide-derived bioprobes have been reported. However, relatively few supply all of the features listed above.

Some typical examples of lanthanide probes include DTPA-cs124, TTHA-cs124, and Lumi4. In the first two probes, a carbostryil dye (cs124) serves as the antenna, while the polyaminocarboxylates DTPA or TTHA coordinate the lanthanide ions (Tb(III) or Eu(III)) (Figure 7C and 7D). Upon complexing to Tb(III), these compounds show extinction coefficients of 10,500 $M^{-1}cm^{-1}$, quantum yields of 0.3 – 0.4, and an absorption maxima of 342 nm.[62] Lumi4 incorporates four hydroxyisophthalamide sensitizers directly into the chelating portion of the molecule (Figure 7B). Lumi4 complexing Tb(III) is the brightest probe so far, with an extinction coefficient of 21000 $M^{-1}cm^{-1}$, quantum yield > 0.5, and an excitation wavelength that peaks at 340 nm and has appreciable absorbance at

365 nm, which is the lowest available wavelength for powerful near-UV, LED light sources.[63]

There are several methods to conjugate these probes to a biological target. Direct conjugation to lysine side-chains via amide bond formation or coupling to a cysteine thiol via a Michael addition reaction with a maleimide group are the most common. For labeling proteins in live cells, the Miller lab has utilized the noncovalent interaction between the antibiotic trimethoprim (TMP) and the enzyme dihydrofolate reductase from *Escherichia coli* (eDHFR).[64] Heterodimers of TMP and lanthanide complexes such as Lumi4 or TTHA-cs124 selectively bind with high affinity (K_d, ~1 nM) to chimeric fusions of eDHFR in cultured mammalian cells or cell lysates.

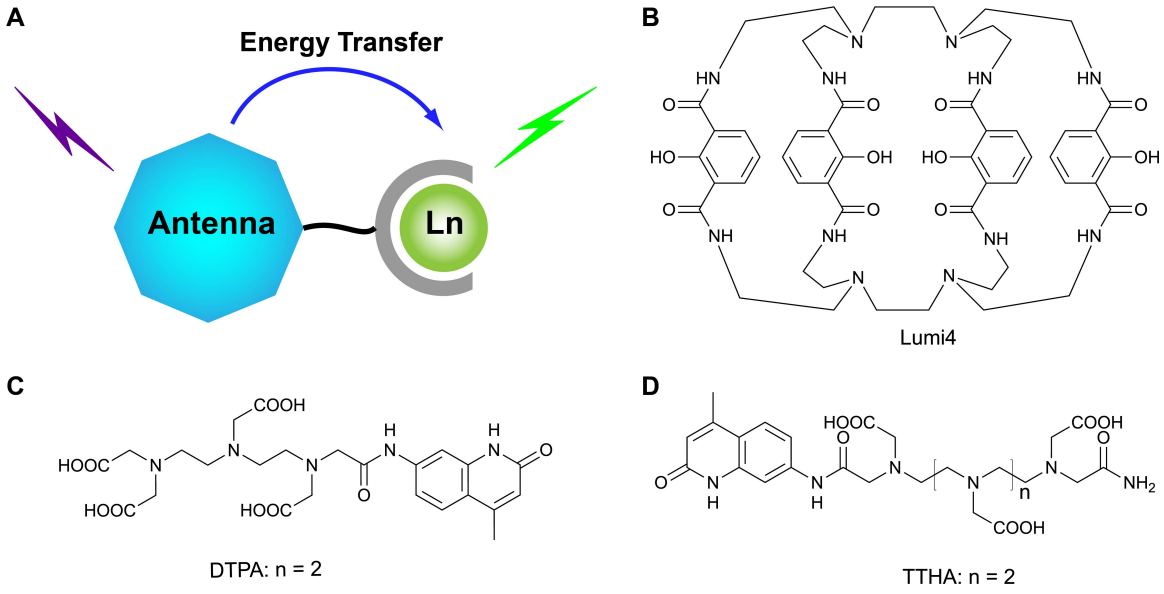

Figure 7. Structure of lanthanide probes. (A) The schematic structure of a lanthanide probe. Chemical structures of (B) Lumi4, (C) DTPA, and (D) TTHA.

1.5.2 Lanthanide complexes in FRET applications

The unique luminescent properties of Tb(III) and Eu(III) complexes offer distinct advantages when used as donors in FRET applications in combination with GFP or other conventional fluorophores (lanthanide-based FRET or LRET). First, the long emission of lanthanides or lanthanide-sensitized GFP can be isolated from background signals using TGL detection. TGL allows pulsed excitation, followed by a brief delay, which eliminates nonspecific fluorescence before the detection of lanthanide-to-GFP emission. As a result, directly excited acceptor fluorescence and autofluorescence background signals are eliminated (Figure 8). Second, bleedthrough is minimized because the narrow emission bands of lanthanides can be spectrally isolated from sensitized acceptor emission signals. Furthermore, long Stokes shifts (> 150 nm) and multiple emission peaks allow for multiplexed LRET, where Tb(III) can sensitize emission of two or more differently colored acceptors. Overall, the ability to temporally and spectrally isolate lanthanide emission signals makes it possible to detect analytes at a small concentration in complex matrixes. As a result, lanthanides are routinely used in HTS using commercial-plate-reader instrumentation. In recent years, there has been considerable interest in leveraging the inherent sensitivity of TGL with Tb(III) and Eu(III) complexes for application in live-cell microscopic imaging. In this study, Tb(III) probes will be used as a donor for our FRET biosensors. These lanthanide-based FRET (LRET) biosensors are used as a tool to study PPIs in both live-cell imaging and HTS.

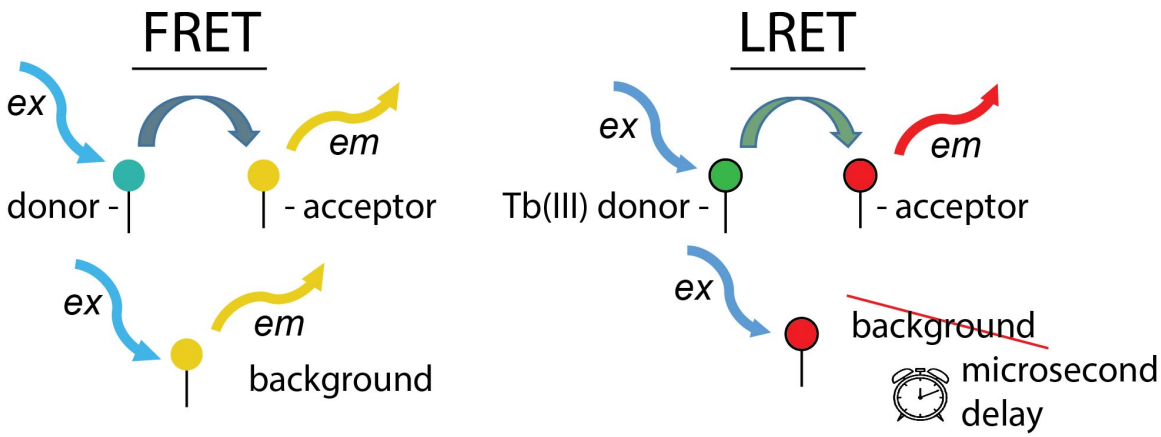

Figure 8. Similarity and differences between FRET and LRET. Background fluorescence often obstructs the measurement of FRET signals. LRET employs lanthanides as the donor and TGL as the detection method. The unique properties of lanthanides temporally and spectrally isolate LRET signals from nonspecific fluorescence.

CHAPTER 2

CHARACTERIZING LRET-BIOSENSOR TOOLKIT WITH FKBP12/FRB MODEL

Some of the work presented in this chapter was performed by Ting Chen, including the cloning of single-chain FKBP12/FRB biosensors, the generation of cell lines stably expressing these biosensors, and the detection of FKBP12/FRB interaction and inhibition in multi-well plates.

2.1 Introduction

PPIs govern pivotal cellular decisions, and abnormal PPIs play a role in many diseases. While understanding PPIs is critical, their discrete and transient nature and spatiotemporal-regulated functions challenge traditional research tools.[2] At this point in time, fluorescence-based biosensors are the most powerful tool for dynamically imaging and analyzing PPIs directly in living cells. With the evolution of FP variants, genetically encoded FP-based, FRET biosensors provide nondestructive and noninvasive visualization of spatiotemporal dynamics of PPIs relative to cells' response to stimuli or changes in phenotypes in live-cell microscopy.[6, 65] Besides imaging, significant efforts have been made in discovering drugs that inhibit or activate PPIs using cell-based screens and counter-assays to evaluate hits or leads for cytotoxicity, membrane permeability, or off-target effects.[66-68]

A key limitation of FRET biosensors is that they often exhibit only a small change in FRET that barely exceeds the noise of many imaging systems and commercial plate readers. I.e., they exhibit a small dynamic range. This chapter will emphasize the design and characterization of a lanthanide-based FRET (LRET) biosensor toolkit that aims to simplify and accelerate the generation of high-dynamic-range biosensors for live-cell imaging and multi-well plate analysis of PPIs. These sensors incorporate a Tb(III) complex as the energy transfer donor and a GFP as the acceptor (Figure 9A-top). Tb and

Tb-to-GFP sensitized emission signals have ms-scale lifetimes that permit the use of time-gated luminescence (TGL) detections. In TGL, pulsed light is used to excite the Tb complex, and sensitized GFP signals are measured after a brief delay (Figure 9A-bottom).[69] Bleedthrough, crosstalk due to overlapping spectrum and ns-scale autofluorescence are therefore minimized. As a result, Off-state FRET signal can be distinguished from On-state FRET signal with a high degree of confidence.

To characterize the performance of biosensors generated by the toolkit, we use the well-characterized rapamycin-induced interaction between FK binding protein 12 (FKBP12) and the rapamycin binding domain of m-Tor (FRB) as a model system. Our dual-chain biosensor design consists of EGFP fused to FKBP12 and eDHFR fused to FRB (Figure 9B). The two biosensor chains were cloned into the same plasmid with dual promoters. Their expression was carefully controlled to minimize stoichiometry artifacts. Our single-chain biosensor consists of FRB, eDHFR, an alpha-helical linker, GFP and FKBP12 (from *N- to C-* terminus) (Figure 9B). The alpha-helical linker helps lessening basal FRET, and is comprised of multiple repeats of four glutamic acid or arginine residues alternated with four lysine residues (ER/K). In both biosensor configurations, the eDHFR domain binds with high specificity and affinity (K_D, ~1 nM) to heterodimers of trimethoprim linked to a luminescent Tb(III) complex,[62] allowing selective labeling of the biosensor construct.

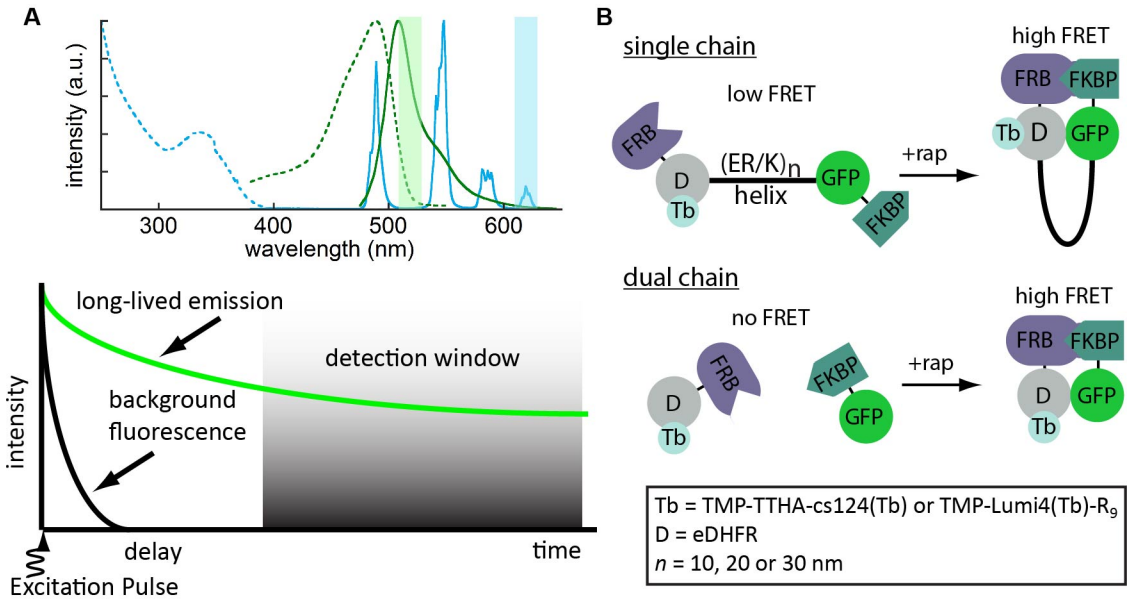

Figure 9. Set-up of the time-gated luminescence (TGL) detection and schematics of dual-chain and single-chain LRET biosensors of FKBP12/FRB interaction. LRET biosensor design leverages the narrow, multi-line emission spectrum and ms-scale excited state lifetime of Tb(III) complexes to facilitate high signal-to-background, time-gated luminescence (TGL) detection. (A) (Top) Excitation (dotted) and emission (solid) spectra of Tb(III) (cyan) and GFP (green). Colored bars show emission bandpass for detecting Tb(III) and Tb(III)-to-GFP FRET signals. (Bottom) Insertion of a delay (10 µs) between pulsed excitation and detection enables background-free detection of Tb(III) luminescence and Tb(III)-to-GFP FRET-sensitized emission. (B) Single-chain biosensor (Top) and dual-chain biosensor design (Bottom). An ER/K helix motif (length 10, 20 or 30 nm) separates FRET partners and affinity pairs in the single-chain configuration. Absent interaction, the ER/K helix maintains affinity and detection elements far apart, ensuring low baseline FRET signal. Stochastic breaking of helix linker permits close approach and binding of affinity domains.

Biosensor activity in NIH3T3 fibroblast cells overexpressing the biosensors was robustly detected in TGL microscopy or TGL analysis in 96-well and 384-well plates. In a time-series image sequence of cells expressing the dual-chain biosensor, the donor-denominated FRET (FRET/Tb) ratio increased to over 250% of its initial value about 5 min after rapamycin addition. When it comes to single-chain biosensors, we observed

extraordinary dynamic ranges of more than 500% and more than 2500% for rapamycin-induced activation of FKBP12/FRB interaction in live-cell microscopic images and 96-well plates, respectively. Furthermore, FKBP12/FRB interaction or inhibition was robustly detected in 384-well plates with statistical significance. The high performance seen here with model systems indicates that the LRET biosensor toolkit can be applied to analyze a wide variety of PPIs.

2.2 Materials and Methods

2.2.1 Materials

NIH 3T3 cells (CRL-1658) were from ATCC. Dulbecco's modified eagle medium with 4.5g/L glucose (DMEM, 10-013CV), Dulbecco's phosphate buffer saline (DPBS, 21-030 and 21-031), and 0.05% trypsin/2.21 mM EDTA (Corning, 25-053-Cl) were purchased from Corning cellgro ®. DMEM (without phenol red, 21063), HEPES (15630-080) and Lipofectamine 2000 (11668-027) were purchased from Invitrogen™. FBS (S11150) was purchased from Atlanta Biologicals. Hygromycin (sc-29067) was purchased from Santa Cruz Biotechnology. BSA (700-107P) was purchased from Gemini Bio-products. Rapamycin (553211-500UG) was purchased from Millipore. Ascomycin (11309) was purchased from Cayman Chemical. NADPH (N0411) and doxycycline (D9891) were purchased from Sigma. DMSO (D128-500) was purchased from Fisher Chemical. Patent V blue sodium salt (21605) was purchased from Fluka. In-Fusion HD cloning kit (638909) was purchased from Takara. All enzymes and buffers used in cloning were purchased from New England Biolabs. TMP-cs124-TTHA-Tb(III) (**1**) was synthesized by Ali Mohamadi. Lumi4-cysTEGTMP-CR9 (**2**) was provided by Lumiphore, Inc (Figure 10).

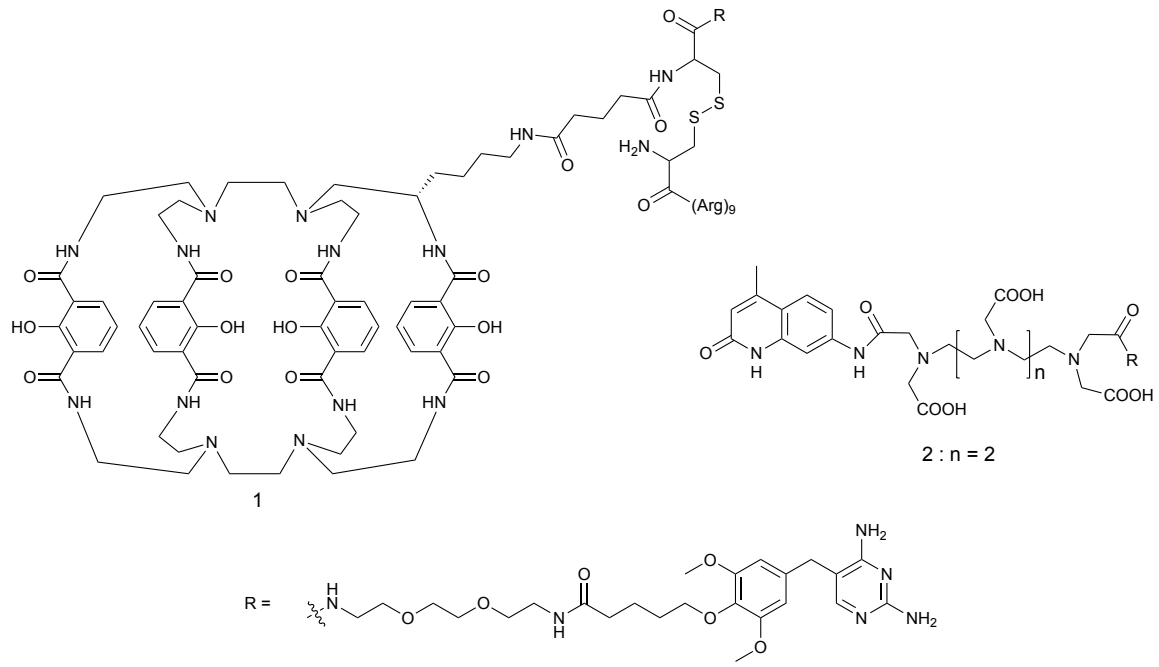

Figure 10. Chemical structures of Tb probes used in the study. Chemical structures of TMP-Lumi4-R9 (1) and TMP-TTHA-cs124 (2). Probe (1) was used in microscopic imaging while (2) was used in plate-reader assay.

2.2.2 Methods

2.2.2.1 Cell culture

NIH-3T3 were maintained in DMEM (4.5 g/L glucose) supplemented with 10% FBS and 15 mM HEPES at 37 °C and 5% CO2. The cells were passaged with 0.05% trypsin/2.21 mM EDTA.

2.2.2.2 Plasmid

pCMV-FKBP12-EGFP and pTREtight-FRB-eDHFR. The gene encoding (CMV Promoter)-EGFP-FKBP-(bGH Poly(A) Signal Sequence) was subcloned from plasmid pEGFP-FKBP12 to pPBH-TREtight-FRB-eDHFR to generate pPBH-TREtight-FRB-eDHFR/GFP-FKBP12. The 1850 bp fragment encoding (CMV Promoter)-EGFP-

FKBP12-(bGH Poly (A) Signal Sequence) was amplified by PCR from pEGFP-FKBP12 using the primers 5' – GCC CGT CCC ACC AGG TGA GTT CCG CGT TAC ATA ACT TAC G – 3' (SexAI, coding strand) and 5' – CGC CTG TTG ACC TGG TCG CGT TAA GAT ACA TTG ATG AG – 3' (SexAI, non-coding strand). This fragment was inserted at the SexAI site in pPBH-TREtight-FRB-eDHFR using In-Fusion® Cloning Kit to give to pPBH-TREtight-FRB-eDHFR/GFP-FKBP12.

pPBH-TREtight-FRB-eDHFR-$(ER/K)_{10nm}$-EGFP-FKBP12. The FRB-eDHFR-$(ER/K)_{10nm}$-EGFP-FKBP12 was prepared by GenScript by synthesizing the open reading frame FRB-eDHFR-$(ER/K)_{10nm}$ -EGFP-FKBP12. The $(ER/K)_{10nm}$ linker has a sequence of 5' – GAA GAG GAA GAG AAA AAA AAA CAG CAG GAA GAG GAA GCA GAA AGG CTG AGG CGT ATT CAA GAA GAA ATG GAA AAG GAA AGA AAA AGA CGT GAA GAA GAC GAA AAA CGT CGA AGA AAG GAA GAG GAG GAA AGG CGG ATG AAA CTT GAG ATG GAA GCA AAG AGA AAA CAA GAA GAA GAA GAG AGA AAG AAA AGG GAA GAT GAT GAA AAA CGC AAG AAG AAG. The synthesized fragment was inserted into pPBH-TREtight vector between KpnI site and NheI site to give pPBH-TREtight-FRB-eDHFR-$(ER/K)_{10nm}$ -EGFP-FKBP12.

pPBH-TREtight-FRB-eDHFR-$(ER/K)_{30nm}$-EGFP-FKBP12. The 630 bp $(ER/K)_{30nm}$ linker fragment was prepared and cloned into pUC57 vector by GenScript . The genes encoding FRB-eDHFR, $(ER/K)_{30nm}$, EGFP-FKBP12 were subcloned from plasmids pPBH-TREtight-FRB-eDHFR-$(ER/K)_{10nm}$-EGFP-FKBP12 and $(ER/K)_{30nm}$ in pUC57 to pPBH-TREtight to generate pPBH-TREtight-FRB-eDHFR-$(ER/K)_{30nm}$ -EGFP-FKBP12. A 753 bp fragment encoding FRB-eDHFR was prepared by PCR from pPBH-TREtight-FRB-eDHFR-$(ER/K)_{10nm}$ -EGFP-FKBP12 using the primers 5'-ACT CTG

CAG TCG ACG GTA CCA TGA TCC TCT GGC ATG AGA TGT GGC -3' (coding strand) and 5'-TCG GAT CCT CCG CTT CCC CGC CG -3' (non-coding strand). A 630 bp fragment encoding $(ER/K)_{30nm}$ was prepared by PCR from $(ER/K)_{30nm}$ in pUC57 using the primers 5'-AAG CGG AGG ATC CGA AGA GGA GGA GAA AAA GAA GGA -3' (coding strand) and 5'-CCA GAG CCA CCG GTT CTC TGT TTT CGC TCT GC -3' (non-coding strand). A 1041 bp fragment encoding EGFP-FKBP12 was prepared by PCR from pPBH-TREtight-FRB-eDHFR-$(ER/K)_{10nm}$-EGFP-FKBP12 using the primers 5'-AAC CGG TGG CTC TGG CAT GGT GAG CA -3' (coding strand) and 5'-ATG CGG CCG CGC TAG-3' (non-coding strand). These 3 fragments were inserted between the KpnI site and the NheI site in pPBH-TREtight by Clontech In-Fusion® Cloning Kit to get pPBH-TREtight-FRB-eDHFR-$(ER/K)_{30nm}$-EGFP-FKBP12.

pPBH-TREtight-FRB-eDHFR-$(ER/K)_{20nm}$-EGFP-FKBP12. The $(ER/K)_{20nm}$ linker is the first 396 bp of $(ER/K)_{30nm}$ linker. The genes encoding FRB-eDHFR, $(ER/K)_{20nm}$, EGFP-FKBP12 were subcloned from plasmids pPBH-TREtight-FRB-eDHFR-$(ER/K)_{10nm}$-EGFP-FKBP12 and $(ER/K)_{30nm}$ in pUC57 to pPBH-TREtight to generate pPBH-TREtight-FRB-eDHFR-$(ER/K)_{20nm}$-EGFP-FKBP12. A 753 bp fragment encoding FRB-eDHFR was prepared by PCR from pPBH-TREtight-FRB-eDHFR-$(ER/K)_{10nm}$ -EGFP-FKBP12 using the primers 5'-ACT CTG CAG TCG ACG GTA CCA TGA TCC TCT GGC ATG AGA TGT GGC -3' (coding strand) and 5'-TCG GAT CCT CCG CTT CCC CGC CG -3' (non-coding strand). A 396 bp fragment encoding $(ER/K)_{20nm}$ was prepared by PCR from $(ER/K)_{30nm}$ in pUC57 using the primers 5'-AAG CGG AGG ATC CGA AGA GGA GGA GAA AAA GAA GGA -3' (coding strand) and 5'-CCA GAG CCA CCG GTC TCT TCC TTG GCC TTT TTC TCC TGC -3' (non-

coding strand). A 1041 bp fragment encoding EGFP-FKBP12 was prepared by PCR from pPBH-TREtight-FRB-eDHFR-$(ER/K)_{10nm}$ -EGFP-FKBP12 using the primers 5'-GAA GAG ACC GGT GGC TCT GGC ATG GTG AGC A -3' (coding strand) and 5'-ATG CGG CCG CGC TAG-3' (non-coding strand). These 3 fragments were inserted between the KpnI site and the NheI site in pPBH-TREtight by Clontech In-Fusion® Cloning Kit to get pPBH-TREtight-FRB-eDHFR-$(ER/K)_{20nm}$ -EGFP-FKBP12.

2.2.2.3 Stable expression of biosensors in mammalian cells

Cells were grown to 70-80% confluency in a sterile 10 cm dish. The cells were transfected with 12 μg of biosensor plasmids and their recombination helper plasmid pSPB-Transposase with a Lipofectamine:plasmid ratio of 2.5μL:1μg per plasmid. Plasmid and Lipofectamine solutions were first prepared in separate microcentrifuge tubes in OptiMEM I with a total volume of 1.5 mL. After 5 minutes of incubation at room temperature, the two solutions were mixed and kept at room temperature for an additional 20 minutes. Afterwards, the cells were incubated with the Lipofectamine - plasmids solution for 4 hours in a tissue culture incubator at 37 ^{o}C and 5% CO_2. The transfection solution was then replaced with 10 mL of fresh DMEM(+) (DMEM supplied with 15 mM HEPES, 10% FBS and 100 mg/mL Hygromycin). The transfections were confirmed by microscopy and/or flow cytometry using the GFP emission.

2.2.2.4 Probe delivery

Cells were trypsinized and seeded at 20,000 cells/well in an 8-well chambered coverglass (Nunc™, 12-565-470) with fresh DMEM (+) containing 100 ng/mL Doxycycline for overnight expression of the biosensor. On the following day, cells were washed twice with DPBS (+Ca/+Mg) and then incubated with 100 μL of TMP-Lumi4-R9

(12 μM in DMEM without phenol red) for 15 min at room temperature, followed by a wash with DPBS (+Ca/+Mg). Next, 150 μL of Rapamycin (1 μM in DMEM without phenol red) was added to sample wells; control wells received 1μM DMSO in DMEM without phenol red. Both sample and control cells were incubated for 15 min at 37 °C and 5% CO_2 incubator, followed by the addition of 20μL of 10 mM patent blue V solution (final concentration: 1 mM) to quench extracellular luminescence from non-specifically adsorbed probe and imaging. To obtain the time-series image sequence, after incubation with the probe solution, cells were first imaged in 10 mM patent blue V solution for before-stimulation images. Rapamycin (final concentration: 2 μM) was then carefully added to cells to keep the same imaging field. Afterwards, the same cells were monitored for post-stimulation images.

2.2.2.5 TGL microscopy and image processing

Time-gated luminescence images were acquired using a previously described epi-fluorescence microscope (Axiovert 200, Carl Zeiss, Inc.).[70, 71] For each time-gated image acquisition, the signal from multiple excitation/emission events was accumulated on the ICCD sensor and read out at the end of the camera frame. The source/camera timing parameters were the same for all time-gated images: excitation pulse width, 1500 μs, pulse period, 3000 μs, delay time, 10 μs, intensifier on-time, 1480 μs. Sensitivity was modulated by either varying the frame length (and thus, the number of integrations) or the intensifier gain voltage; all data reported here was acquired at a gain of 833 V. The camera control software enabled summation of multiple frames to yield a single composite. TIFF image with a bit depth equal to 1024 multiplied by the number of frames. All images reported here were summations of four frames (bit depth, 4096), and

a feature of the camera control software was enabled that removes large variations in signal resulting from ion-feedback noise of the intensifier. The emission filters for each channel were as follow: 620/20 for Tb, 520/20 for FRET and 535/50 for GFP channel.

Raw, 12-bit images were imported into NIH ImageJ (v1.42q) for all processing operations including cropping, contrast adjustment, and quantitative analysis.[72] For each channel, 20 dark frames and 20 bright field images were stacked, converted to 32 bits, and median-filtered (radius 1), and each stack was averaged. The flat-field average was divided by the mean intensity of its central nine pixels to generate a normalized flat-field image. For each sample image, a median filter (radius 1) was applied and the master dark frame was subtracted. The resulting image was then divided by the normalized, master flat-field image, and the mean value of the detector offset was added back to the image. For ratiometric images and measurements, a binary mask was created by first averaging a series of GFP images and then applying a threshold to highlight only regions exhibiting signal. The mask was applied to background-subtracted time-gated FRET images, and the FRET images were then divided by the GFP or Tb image. Intensity-modulated ratiometric displays were generated using the Fire lookup table in ImageJ and a color lookup table was applied.

2.2.2.6 Rapamycin stimulation assay with permeabilized mammalian cells

Cells stably transfected with the biosensor were seeded at a density of 1.6×10^5 cells/mL in a multi-well plate (250 μL for 96-well plate, 50 μL for 384-well plate). Following an overnight incubation with 100 ng/mL doxycycline for biosensor expression, growing media in each well was discarded carefully an lysis buffer containing 25 nM TMP-cs124-TTHA-Tb^{3+}, 5 μM NADPH, 0.1% BSA, 0.1% Triton X-100 and 1 μM

rapamycin in DPBS solution was added to each well (50 µL for 96-well plate, 30 µL for 384-well plate). The plate was then incubated at room temperature for 15 min in a dark place before taking the measurement. Negative control wells contained no cells, but only the same lysis buffer as sample wells.

2.2.2.7 Ascomycin inhibition assay with permeabilized mammalian cells

Cells stably transfected with the biosensor were seeded at a density of 1.6×10^5 cells/mL in a multi-well plate (250 µL for 96-well plate, 50 µL for 384-well plate). Following an overnight incubation with 100 ng/mL doxycycline for biosensor expression, growing media in each well was discarded carefully an lysis buffer containing 50 nM TMP-cs124-TTHA-Tb^{3+}, 5 µM NADPH, 0.1% BSA, 0.1% Triton X-100, 0.333 µM rapamycin and 20 µM ascomycin in DPBS solution was added to each well (50 µL for 96-well plate, 30 µL for 384-well plate). The plate was then incubated at room temperature for 15 min in a dark place before taking the measurement every 10 min for 2.5 hours. Negative control wells contained cells without protein expression, but the same lysis buffer as sample wells.

2.3 Results and Discussion

2.3.1 Biosensor Design

Unlike with single-chain formats, dual-chain biosensor design is straightforward and helps enhance the sensor sensitivity because affinity domains are fully separated in the sensor Off-state. However, the distribution of the two biosensor components in the cell is not uniform, and variation in the local concentration of donors and acceptors must be corrected with additional images and post-acquisition image processing. Here, we used a dual-promoter vector for the expression of the two sensor chains from a single

plasmid. We carefully controlled the expression level of each sensor chain to minimize stoichiometry artifacts. Specifically, NIH 3T3 cells were stably transfected with a PiggyBac plasmid vector that encoded the fusion protein EGFP- FKBP12 under control of a CMV promoter for continuous expression and FRB-eDHFR under control of a pTREtight promoter for doxycycline-induced expression (Figure 11d). Following transfection and growth selection to engender stable expression, cells were sorted to obtain a population with similar GFP expression level. Next, FRB-eDHFR expression levels were optimized by determining the doxycycline concentration necessary to see the maximum FRET signal. Because of the large Stokes shifts and narrow emission lines of Tb(III) and the elimination non-specific fluorescence by time-gating, the level of bleed-through or crosstalk in the FRET channel was negligible (< 5%).

In general, single-chain biosensors can be easily expressed in cells through the transfection of a single plasmid and require simple ratiometric image analysis. Most commonly, intrinsically unstructured linkers are incorporated into single-chain biosensors so as to avoid unfavorable dipole-dipole orientations between donor and acceptor chromophores when the sensor is in the closed, or high-FRET state. However, single-chain sensors may adopt off-state conformations that lead to high FRET baselines and reduce dynamic range. This artifact is potentially a bigger problem for single-chain LRET biosensors because FRET between lanthanides and fluorescent proteins can be observed over relatively long distances (10 – 20 nm) compared to conventional FRET.[73] Therefore, the middle linker of a single-chain LRET sensor should ideally be able to regulate the interchromophore distance (r): shorter r in the more compact state and longer r in the less compact state. This design may be pursued without concern for linker effects

on dipole orientation because Tb(III) or Eu(III) emits multiple dipole moments at many different orientations.[74]

To reduce baseline FRET signals, a semi-rigid α-helix linker sequence which consists of an alternating sequence of approximately four glutamic acid residues followed by approximately four arginine or lysine residues [$(E/R)_4/K_4$, or ER/K linker) was incorporated into our sensor design. The linker was reported to adopt an alpha-helical geometry in solution and effectively regulate protein interaction in so-called SPASM sensors.[75] Specifically, our sensor consists of (from N-to-C terminus) FRB, eDHFR, ER/K, GFP, and FKBP12 placed under the control of Tet-responsive promoter (Figure 9B). We generated three biosensors with ER/K linker lengths of 10 nm, 20 nm, or 30 nm. The ER/K linker helps lower basal FRET by keeping each end of the inactive sensor at rigid distances and orientations from one another while breaking stochastically to permit close approach of elements positioned on either end. Because the fraction of an ER/K biosensor in the closed state depends merely on linker length and the K_D of the sensing elements, we may detect PPIs even when the overall sensor concentration is far below the K_D.[76]

2.3.2 TGL microscopy of biosensors in live cells

We created four stably transformed cell lines that expressed the dual-chain sensor or single-chain sensors with ER/K linker lengths of 10 nm, 20 nm, or 30 nm. Following an overnight induction of biosensor expression with doxycycline, cells were incubated in culture medium containing 12 μM of a cell-permeable luminescent Tb(III) complex, TMP-Lumi4-R_9 (Figure 10) at room temperature. After 15 min, cells were washed two times with PBS, immersed in imaging medium, and then imaged immediately.

Continuous-wave images of GFP fluorescence revealed the distribution of single-chain or dual-chain biosensors throughout the cytoplasm (Figure 12A) or cytoplasm and nucleus (Figure 11a), respectively. These distribution patterns agree with the size of each biosensor: single-chain biosensors are relatively large and therefore excluded from the nucleus. Time-gated images of Tb(III) luminescence and Tb(III)-to-GFP sensitized emission revealed Tb(III) probe distribution throughout the cytoplasm and nucleus for all four biosensors (Figure 11a and Figure 12A).

Ratiometric images showed that our LRET biosensors enabled sensitive detection of FKBP12/FRB interaction in live cells. Substantial increases in both FRET/Tb and the acceptor-denominated FRET ratio (FRET/GFP) were observed in rapamycin-stimulated cells expressing biosensors. Specifically, in a time-series image sequence of cells expressing the dual-chain biosensor, an increase in FRET/GFP ratio of about 271 ± 41% (mean ± s.e.m) was observed for an 11-cell sample after 5 min of rapamycin addition (Figure 11b and c). When it comes to single-chain biosensors, the dynamic range of both FRET/Tb and FRET/GFP signals increased with linker length and biosensors with 20 nm and 30 nm ER/K linkers possessed higher microscopic dynamic range than the dual-chain biosensor. The maximum, microscopically observed increases in mean FRET/GFP were 61%, 378%, and 470% for linker lengths of 10, 20, and 30 nm, respectively (Figure 12C-left). While the values in mean FRET/Tb were 87%, 288%, and 525% for cells expressing sensors with 10, 20, and 30 nm ER/K linkers, respectively (Figure 12C-right). In addition, a time-series image sequence of cells expressing the single-chain biosensor with 20 nm ER/K linker illustrated increasing FRET efficiency overtime after rapamycin stimulation (Figure 12B).

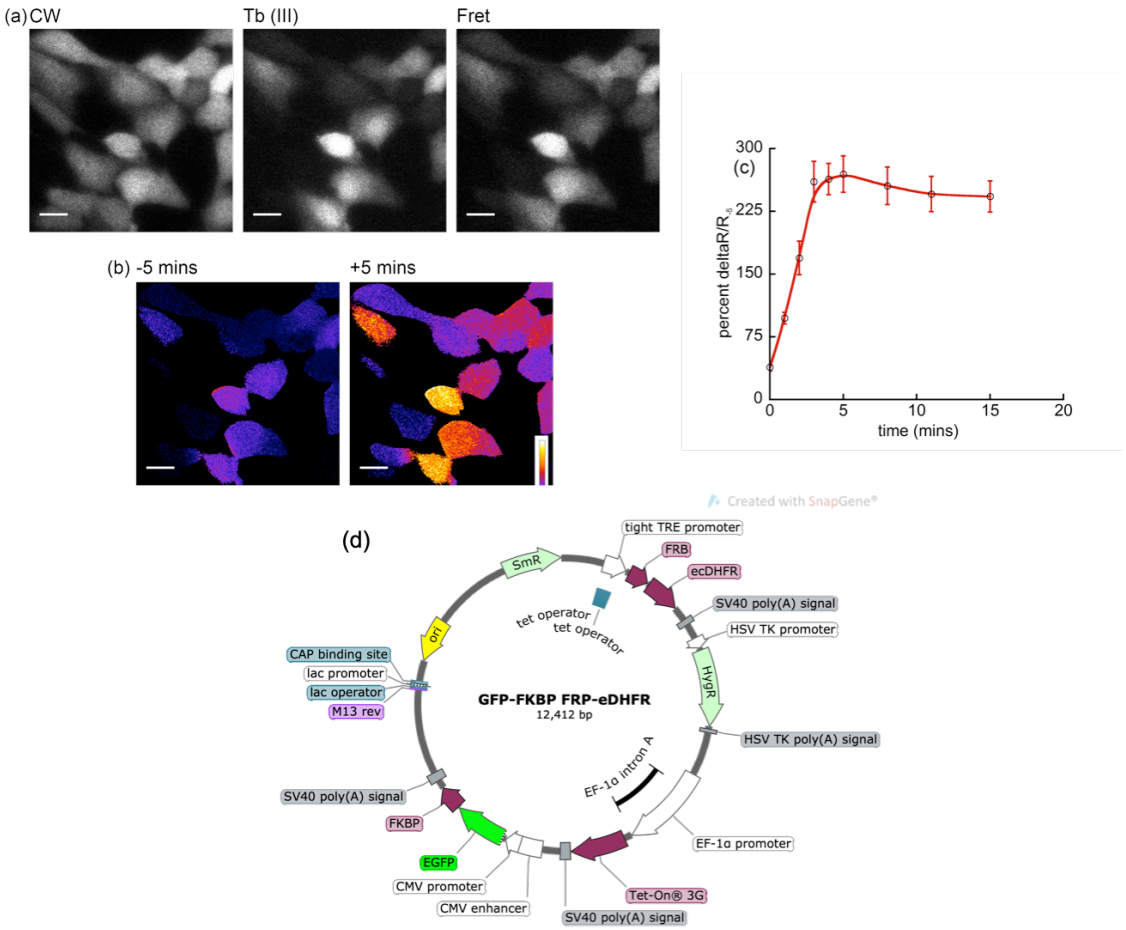

Figure 11. Time-gated luminescence microscopy of the dual-chain FRET biosensor. (a) Representative images of NIH3T3 fibroblasts cells stably expressing the sensor. Micrographs: CW, steady-state fluorescence (λ_{ex} 480 nm, λ_{em} 535 nm); Tb(III), time-gated Tb(III) luminescence (λ_{ex} 365 nm, λ_{em} 620 nm, gate delay 10 μs); FRET, time-gated Tb(III)-to-GFP sensitized emission (λ_{ex} 365 nm, λ_{em} 520 nm, gate delay 10 μs). Scale bar, 20 μm. (b) Ratio images (FRET/CW) before (left) and after (right) addition of rapamycin. (c) Percent increase of FRET/CW at different time points after adding rapamycin ($\Delta R/R_{-5}$). Values given are averaged from 11 cells. Error bars, SEM. (d) A dual-promoter PiggyBac plasmid vector that encoded the fusion protein EGFP- FKBP12 under control of a CMV promoter for continuous expression and FRB-eDHFR under control of a pTREtight promoter for doxycycline-induced expression.

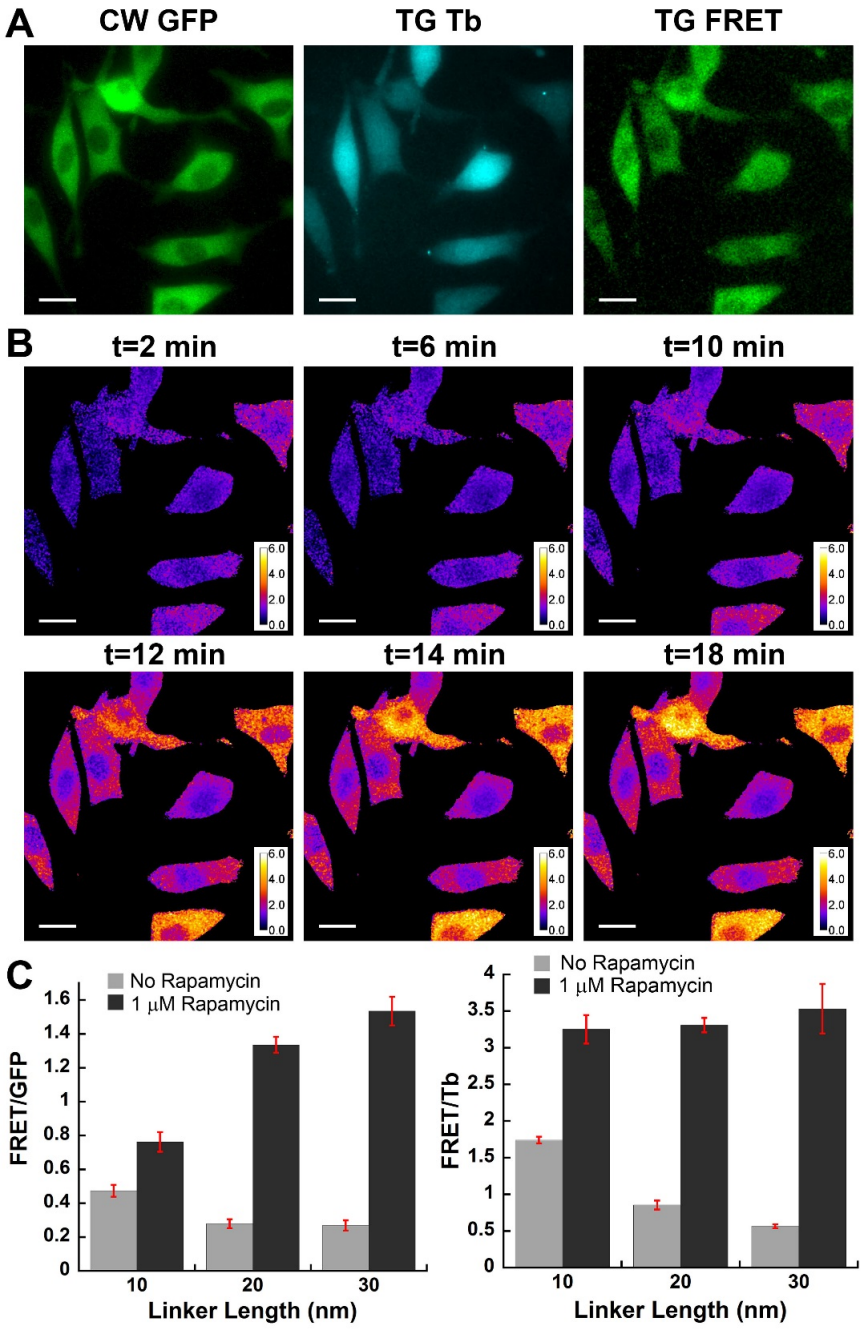

Figure 12. Time-gated luminescence microscopy of single-chain FRET biosensors. (A) Representative images of NIH3T3 fibroblasts cells stably expressing FRB-eDHFR-$(ER/K)_{20}$-GFP-FKBP12 approximately 20 min after stimulation with 1 μM rapamycin. Micrographs: CW GFP, steady-state GFP fluorescence (λ_{ex}, 480 ± 20 nm; λ_{em}, 535 nm ± 25 nm); TG Tb, time-gated Tb(III) luminescence (λ_{ex}, 365 nm, λ_{em}, 620 nm ± 10 nm, gate delay 10 μs); TG FRET, time-gated Tb(III)-to-GFP sensitized emission (λ_{ex}, 365 nm; λ_{em}, 520 ± 10 nm, gate delay 10 μs). Scale bar, 20 μm. Tb and FRET channel images were rendered at identical contrast. (B) Color maps of the same cells shown in A depict the ratio of the TG FRET image to the TG-Tb image at various time points following rapamycin stimulation. (C) Biosensor dynamic ranges increase with the length of ER/K

linker due to reduction in baseline, or Off-State FRET signals. Bar graphs depict the mean, pixel-wise FRET/Tb or FRET/GFP ratios measured in regions of interest drawn within cells both before and 25 min after addition of rapamycin. Values given are averaged from 10 or more cells for each condition. Error bars, SEM.

2.3.3 Detection of PPIs and their Inhibition in Multi-well plates

In general, FRET-based detection of cellular PPIs is seldom used at medium-to-high throughput due to the aforementioned limitations. Here, we evaluate the potential of our LRET biosensors for the detection and quantification of PPIs and their inhibition in multi-well plates with cell-based format. Owing to the superior of the single-chain LRET biosensors to the dual-chain sensor in terms of microscopic dynamic range and simplicity in expression, we used single-chain biosensors for this purpose. NIH 3T3 cells stably expressing single-chain, FKBP12/FRB biosensors were seeded into 96-well plates (40,000 cells/well) or 384–well plates (8000 cells/well) and grown overnight in medium containing doxycycline to induce protein expression. Following incubation, lysis buffer containing 1 μM rapamycin and TMP-TTHA-cs124(Tb) (final conc., 25 nM) was added to the wells, the plate was incubated at room temperature. The amount of rapamycin was determined from a titration assay to maximize FKBP12/FRB interaction. After 15 min incubation with the lysis probe solution, the time-gated Tb(III) and Tb(III)-to-GFP FRET emission signals were measured and normalized to obtain FRET/Tb ratio for each well. The mean FRET/Tb ratio from control wells containing non-expressing cells and lysis buffer with TMP-cs124-TTHA(Tb) but lacking rapamycin was subtracted from the FRET/Tb ratio from sample wells. The background-corrected, FRET/Tb ratio represented

for the FRET efficiency in each well with minimum artifacts from well-to-well variability in probe amounts or sample absorbance.

Similar to microscopy data, the dynamic ranges of single-chain biosensors increase with linker length but in much higher magnitude. In 96-well plate assay, cells expressing FKBP12/FRB biosensors with 10 nm, 20 nm, or 30 nm ER/K linkers presented dynamic ranges of 165%, 1700%, and 2500%, respectively (**Figure 13A**). For all sensor constructs, the maximum observed FRET/Tb ratio was similar. However, the sensor with 10 nm ER/K linker had a higher baseline FRET signal. In addition, the Z' factor ranged from 0.72 to 0.89 for all sensors, indicating a highly robust assay. As for 384-well plates, substantial larger FRET/Tb ratios were observed in the positive control wells (1 μM rapamycin) relative to those seen in the negative controls (no rapamycin). However, Z' factor for 384-well plate assay was relatively poor with the value of about zero for the sensor with the 10 nm ER/K linker and 0.41 for the sensor with the 30 nm ER/K linker. Further improvement in assay robustness may be achieved with optimization to remove variance from manual plate preparation.

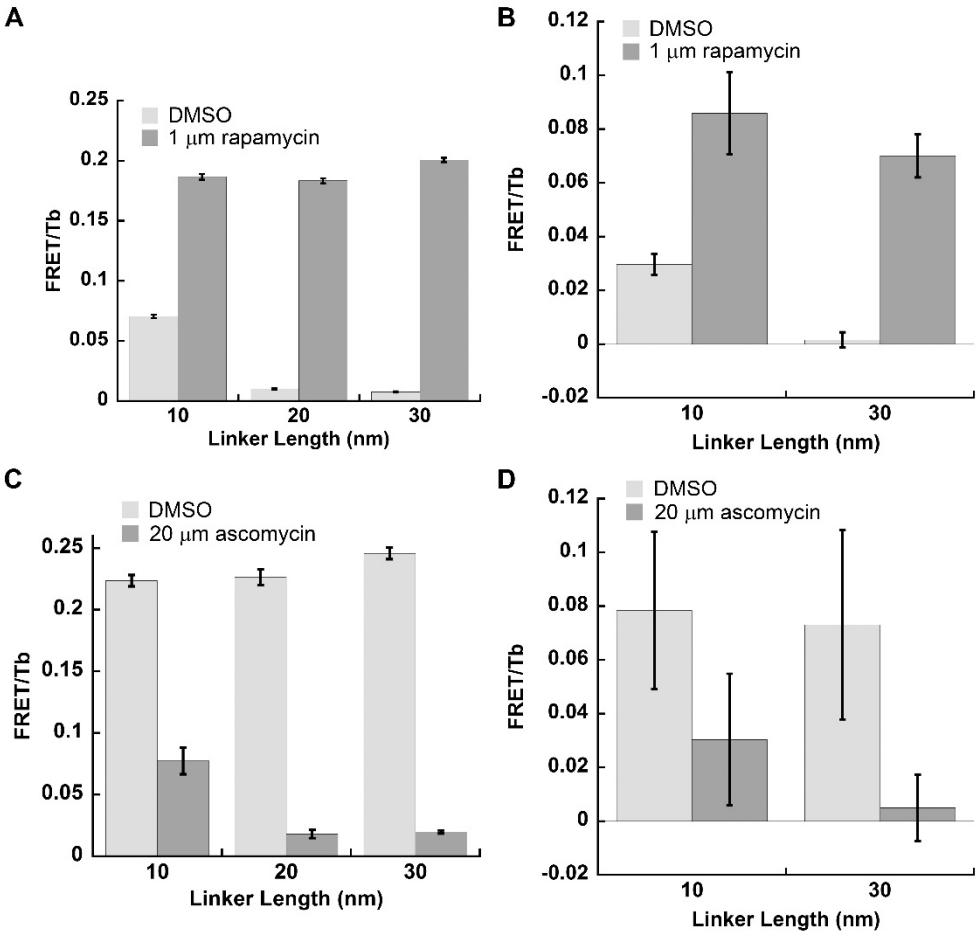

Figure 13. TGL analysis robustly detects FKBP12/FRB interaction and its inhibition following permeabilzation of sensor-expressing cells grown in multiwell plates. NIH 3T3 fibroblast cells expressing FKBP12/FRB sensor were grown in 96-well (A, C) or 384-well (B, D) plates at cell densities of 40,000 or 8,000 cells/well, respectively. (A, B) Following overnight incubation, cells were treated with lysis buffer containing TMP-TTHA-cs124 (25 nM) and, for positive control wells, rapamycin (1 μM). The time-gated emission (gate delay, 0.2 ms) at 520 nm (Tb-to-GFP FRET) and 620 nm (Tb only) were measured using a time-resolved fluorescence plate reader. Substantial larger FRET/Tb ratios were observed in the positive control wells (1 μM rapamycin) relative to those seen in the negative controls (no rapamycin). (C, D) Cells were treated with lysis buffer containing TMP-TTHA-cs124 (25 nM), rapamycin (0.33 uM) and, for positive control wells, ascomycin (20 uM). Time-gated signals were then measured as in (A, B). FRET/Tb emission ratios were observed to decrease by more than 60% for all sensor linker lengths in both 96-well and 384-well plates. Bar graphs depict mean FRET/Tb ratio measured for positive controls (n = 16) and for negative controls (n = 8). Error bars, SD. Data were collected by Ting Chen.

To further assess the potential of LRET biosensors for multi-well plate applications, we studied the effects of ascomycin as an inhibitor of the rapamycin-induced FKBP12/FRB interaction.[77] Ascomycin inhibition assay was performed with a similar set up to the above activation assay. The only difference was the lysis buffer, which contained TMP-TTHA-cs124 (25 nM), rapamycin (0.33 uM), and, for positive control wells, ascomycin (20 uM). The amount of ascomycin was determined from a titration assay for full inhibition. After ascomycin inhibition, background-subtracted FRET/Tb signal decreased more than 60% for all ER/K linker lengths. Excellent Z' values (greater than 0.69) were obtained for all 96-well plate assay conditions. However, negative Z' values were calculated for all 384-well plate assays. Again, manual plate preparation may introduce data variance.

2.4 Conclusion

Lanthanide-based FRET can adopt both dual-chain and single-chain design to generate LRET biosensors with remarkable dynamic ranges in TGL microscopy. The narrow emission peaks and large Stokes shift of lanthanide probes and the use of a dual promoter plasmid for optimum expression of biosensor components simplify the complex image analysis associated with the dual chain configuration. On the other hand, the time-gated elimination of non-specific fluorescent signals and the incorporation of a rigid alpha-helical linker structure into the biosensor to hold two biosensor ends far apart in Off-state generate single-chain biosensors with excellent dynamic ranges. Together with the simplicity in expression and analysis, single-chain LRET biosensors are preferred so long as the linking of two affinity domains does not cost any geometrical constraint. In addition, a consistent trend for linker length was observed in both microscopic and plate

reader data: dynamic range of the sensor increase with ER/K linker length owing to a reduction in basal FRET.

As for plate reader data, single-chain LRET sensors make it possible to detect PPIs or their inhibition in the cell-based platform at medium-to-high throughput. Biosensors with 20 nm or 30 nm linker length showed substantial FRET signal changes and low variability when detecting FKBP12/FRB interaction and its inhibition in 96-well assay following permeabilization of expressing cells. Large differences but low Z' factors were observed for the same assay at high throughput. Further improvement in assay robustness may be achieved with optimization to remove variance from manual plate preparation. The ability to detect PPIs in cell-based 96-well assays and the potential of 384-well assays will enhance drug discovery efforts by simplifying assay protocols and enabling access to a wider variety of PPIs than cannot be analyzed using assays with purified components. Altogether, the outcomes displayed here show that LRET biosensors are versatile for studying PPIs and their function in live cells.

CHAPTER 3

RAC1 BIOSENSORS FOR IMAGING AND HTS

3.1 Introduction

Rac1, a member of the Rho family of GTPases, is well recognized for controlling a diverse range of cellular processes.[78] It is a key regulator in actin remodeling, adherence junction formation, and establishment of cell polarity.[79] In addition, Rac1 is also involved in transcriptional activation,[80] cell cycle progression,[81] G2/M checkpoint activation, and DNA damage response.[82, 83] These diverse functions of Rac1 require a complex regulation of its subcellular location and interactions with multiple downstream targets.[84] Understanding the molecular regulation of Rac1 is important because their roles are critical both in normal cellular functions and in many diseases.

Over the past ten years, rapid progress has been made in understanding Rac1 signaling, and FRET biosensors have played a vital role in quantifying the spatiotemporal dynamics of the Rac1 nucleotide-binding state in living cells. In 2000, Kraynov et al. developed the first dual-chain Rac1 biosensor called FLAIR to monitor the interaction between two protein domains, Rac1 fused to GFP and the p21-binding domain (PBD) of Pak1 labeled with Alexa546.[41] Pak1 is a downstream effector that binds to the active state of Rac1. Rac1 is activated by the release of guanine diphosphate (GDP) and the loading of guanine triphosphate (GTP), which is catalyzed by upstream regulator guanine nucleotide exchange factors (GEFs).[85] Besides GEFs, other major regulators which control Rac1 GTP/GDP binding status are GTPase activating proteins (GAPs) which accelerate the hydrolysis of GTP into GDP to turn Rac1 off [86] and guanine nucleotide dissociation inhibitors (GDIs) which bind to GDP-associated Rac1 and chaperone it in the cytoplasm in an inactive state.[87] It is important to retain the Rac1 C-terminal CAAX box for membrane localization and interaction with GDI. As a result, Rac1 should be

placed at the C-terminus of the biosensor. The activity of Rac1 biosensors may be evaluated by co-expressing them with both positive and negative regulators.

Considerable efforts have been made in designing and optimizing Rac1 biosensors since the report of the first sensor in 2000. First, the dual-chain configuration was replaced by single-chain designs as in Raichu Rac1 and later biosensors to overcome the complexity in data analysis. Then, to cope with the low sensitivity of the single-chain model, linker sequences were engineered for better separation of affinity elements and fluorophores in the low-FRET state. In addition, different FP variants, including cpFPs were screened to identify Rac1 biosensors with increased dynamic range. Overall, current single-chain FRET Rac1 biosensors exhibit low to medium dynamic range (40-150%) (see chapter 1). The sensor design consisting of a donor FP, PBD, a short linker sequence, an acceptor FP, and Rac1 is commonly used to retain Rac1 interaction with GDI for its spatiotemporal dynamics.

Overexpression of Rac1 and its hyper-activation caused by overexpression of Rac1 specific GEFs such as Tiam1 and Vav1 have been observed in various tumor types, including pancreatic cancer.[88, 89] Rac1 activates multiple signaling pathways that lead to uncontrolled proliferation, invasion and metastasis.[90] As a result, targeting Rac1, especially its GEF-binding site, is a viable therapeutic strategy for many cancers. In fact, several small molecules have been reported as Rac1 inhibitors,[91-95] such as NSC23766 identified as a specific inhibitor of a subset of GEF binding to Rac1[94] and EHT 1864 which inhibits Rac1 by altering the nucleotide-binding site.[95] At this point in time, small molecule inhibitors that target Rac1 have been identified through structure-based virtual high throughput screening,[91, 93] followed by pull-down assays to examine hits.[96, 97]

Although this method is realizable, the technical complication, high cost, and the missing of native environment during screening are among its disadvantages. Furthermore, activation of Rac1 in Rac1 pull-down assay is usually by growth factors (EGF, PDGF) or other extracellular stimuli, which triggers a multitude of parallel signaling pathways and significantly complicates the analysis of individual Rac1 activation.

Here, the LRET biosensor toolkit was applied to develop Rac1 biosensors with enhanced dynamic range that are suitable for either live cell microscopy or cell-based screening in multi-well plates. The performance of the novel biosensors was benchmarked against prior designs reported in the literature. We examined two key performance parameters, ER/K linker length and FRET/LRET donor and acceptor photophysical properties. We built a series of nine biosensors that incorporated Rac1 at the C-terminus, ER/K linkers of various lengths (10 nm, 20 nm, and 30 nm) and three different FRET pairs: an FP pair - Ypet/mCerulean, a cpFP pair - mTFP1(cp227)/Venus(cp229), and an LRET pair - Tb(III) probe/GFP. Overexpression of the biosensor and negative (RhoGDI) or positive (Tiam1) regulators in 293T cells enabled the determination of sensor dynamic range. Remarkable dynamic ranges of ca. 600% and ca. 1100% were observed in LRET biosensors with 20 nm or 30 nm ER/K linkers in 96-well plates, respectively. While significantly improving the dynamic range of LRET biosensors, ER/K linker length imposed a marginal effect on FP and cp-FP Rac1 biosensors with a maximum dynamic range of 125% observed in Ypet/mCerulean sensor with 20 nm ER/K linker. Live-cell microscopic images of this FP biosensor showed robust Rac1 activation near protruding edges of stimulated cells following activation. Notably, the LRET biosensor with 30 nm ER/K linker was successfully

applied in cell-based 96-well inhibition assays. In these assays, Tiam1 was used for specific Rac1 activation mimic the overexpression of this regulator in cancer cells. Large differences and excellent Z' factors were observed in the inhibitor assay with EHT1864, a Rac1 specific inhibitor.

3.2 Materials and Methods

3.2.1 Materials

293T cells (CRL-3216), HeLa cells (CCL-2), and MEF cells (SCRC-1040) were from ATCC. Dulbecco's modified eagle medium with 4.5g/L glucose (DMEM, 10-013CV), Dulbecco's phosphate buffer saline (DPBS, 21-030 and 21-031), and 0.05% trypsin/2.21 mM EDTA (Corning, 25-053-Cl) were purchased from Corning cellgro ®. DMEM (without phenol red, 21063), HEPES (15630-080) and Lipofectamine 2000 (11668-027) were purchased from Invitrogen™. FBS (S11150) was purchased from Atlanta Biologicals. Hygromycin (sc-29067) was purchased from Santa Cruz Biotechnology. BSA (700-107P) was purchased from Gemini Bio-products. Rapamycin (553211-500UG) and Fibronectin bovine plasma (F1141) were purchased from Millipore. NADPH (N0411) and doxycycline (D9891) were purchased from Sigma. DMSO (D128-500) was purchased from Fisher Chemical. Patent V blue sodium salt (21605) was purchased from Fluka. In-Fusion HD cloning kit (638909) was purchased from Takara. All enzymes and buffers used in cloning were purchased from New England Biolabs. pUSE-RapR-Src-as2-mCherry-myc and pUSE- ipep-FRB* plasmids were a gift from Dr. Andrei Karginov's lab.

Luminescent Tb(III) complexes. Heterodimers of trimethoprim linked to luminescent Tb(III) complexes (TMP-cs124-TTHA,[62, 98] and TMP-Lumi4[62]) and a cell

permeable variant conjugated to oligoarginine (TMP-Lumi4-R_9)[99] were prepared as previously reported.

3.2.2 Methods

3.2.2.1 Cell culture

HeLa cells were maintained in DMEM (1.0 g/L glucose) supplemented with 10% FBS, 1X MEM non-essential amino acids and 15 mM HEPES at 37 °C and 5% CO2. The cells were passaged with 0.25% trypsin/2.21 mM EDTA.

293T cells were maintained in DMEM (4.5 g/L glucose) supplemented with 10% heat-inactivated FBS and 2mM L-glutamine at 37 °C and 5% CO2. The cells were passaged with 0.05% trypsin/2.21 mM EDTA.

NIH 3T3 cells were maintained in DMEM (4.5 g/L glucose) supplemented with 10% FBS at 37 °C and 5% CO2. The cells were passaged with 0.05% trypsin/2.21 mM EDTA.

3.2.2.2 Plasmid

pTriEX-Ypet-PBD-$(ER/K)_n$-mCerulean-Rac1 (n = 10nm, 20nm, or 30 nm) was prepared by subcloning from pTriEX-Ypet-PBD-mCerulean-Rac1. The source vector was provided by Hahn lab at the University of North Carolina at Chapel Hill. HindIII to NotI fragments encoding 10 nm, 20 nm, or 30 nm ER/K linker were amplified using the following primer pairs respectively: 5'-ACT GAA GCT TCA GGA AGC GGA GAA GAG GAA GAG A-3' and 5'-TGA TGC GGC CGC CAG AGC CCT TCT TCT TGC G-3'; 5'-ACT GAA GCT TCC GGA GGA TCC GAA GAG GAG GA-3' and 5'-TAA TGC GGC CGC CAG AGC CAC CGG TCT CT-3'; 5'-AGC AAA GCT TCT GGA TCC GAA GAG GAG GAG A-3' and 5'-CTT AGC GGC CGC CAC CGG TTC

TCT GTT TTC GC-3'. The linker fragment was then inserted between the HindIII site and the NotI site in the source vector.

pTriEX4-mTFP1/cp227-PBD-(ER/K)$_n$-Venus/cp229-Rac1 (n = 10nm, 20nm, or 30 nm) was subcloned from pTriEX4-mTFP1/cp227-PBD-Venus/cp229-Rac1. The source vector was purchased from Addgene. XmaI to NotI fragments encoding 10 nm, 20 nm or 30 nm ER/K linker were amplified using the following primer pairs respectively: 5'-TAA TCC CGG GGG AAG CGG AGA AGA GGA AG-3' and 5'-TAA TGC GGC CGC GCC AGA GCC CTT CTT CTT GC-3'; 5'-TAA TCC CGG GGG AGG ATC CGA AGA GGA GGA GAA-3' and 5'-TAA TGC GGC CGC AGA GCC ACC GGT CTC TTC-3'; 5'-CGT ACC CGG GGG AGG ATC CGA AGA GGA GGA-3' and 5'-CTT AGC GGC CGC ACC GGT TCT CTG TTT TCG-3'. Those fragments were then inserted between the XmaI site and the NotI site in the source vector.

pTriEX4-EGFP-PBD-(ER/K)$_n$-eDHFR-Rac1 (n = 10nm, 20nm, or 30 nm) was subcloned by replacing mTFP1/cp227 and Venus/cp229 in pTriEX4-mTFP1/cp227-PBD--(ER/K)$_n$-Venus/cp229-Rac1 with EGFP and eDHFR. The EGFP fragment was subcloned between NcoI and BspEI sites using the primer pair: 5'-TCG CCA CCA TGG TGA GCA AG-3' and 5'-TTC GAA GCT TGA GCT CGA GAT CTG-3'. The eDHFR fragment was subcloned between NotI and KpnI sites using the primer pair: 5'-ATG CAG CGG CCG CCA TGA TCA GTC TGA TTG CGG CGT TA-3' and 5'-ATC GAG GTA CCA GAC CGC CGC TCC AGA ATC TCA-3'.

Doxycycline-inducible constructs. To generate **pPBH-TRE$_{tight}$-mTFP1/cp227-PBD-(ER/K)$_{20}$-Venus/cp229-Rac1**, the entire biosensor cassette was subcloned to PiggyBac Transposon vector system (SBI System Biosciences) by In-Fusion HD cloning

kit. The biosensor construct was amplified using the primer pair: 5'-ACT CTG CAG TCG ACG GTA CCT TAT TTA CAA TCA AAG GAG ATA TAC CAT GGT GAG C-3' and 5'-AGC TTA TCG ATG CGG CCG CGG ATA GGC AGC CTG CAC CTG A-3'. To generate **pPBH-TRE$_{tight}$-EGFP-PBD-(ER/K)$_{30}$-eDHFR-Rac1**, the gene encoding PBD-30nm ER/K linker, and eDHFR-Rac1 were subcloned with infusion primers to a PiggyBac vector containing EGFP. A 918 bp fragment encoding PBD-30nm ER/K linker was amplified by PCR using the infusion primers 5'- ACT CTG CAG TCG ACG GTA CCT CCG GAC TCA GAT CTG AGC TC-3' and 5'- CTG ATC ATG CCA GAA CCG GTT CTC TGT TTT CGC TCT-3'. A 1071 bp fragment encoding eDHFR-Rac1 was amplified by PCR using the infusion primers 5'- TTC TGG CAT GAT CAG TCT GAT TGC GGC G-3' and 5'- ATG CGG CCG CGC TAG CCT ACA ACA GCA GGC ATT TTC TCT TCC-3'. These two fragments were inserted between the KpnI site and the NheI site the destination vector by infusion enzyme. Plasmid integrity was confirmed by direct sequencing. To generate the dual-promoter plasmid: **pPBH-TRE$_{tight}$-RapR-Src-as2-mCherry-myc and pCMV-ipep-FRB***, the gene encoding RapR-Src-as2-mCherry-myc and (CMV Promoter)- ipep-FRB*-(bGH Poly(A) Signal Sequence) from pUSE-RapR-Src-as2-mCherry-myc and pUSE- ipep-FRB*, respectively, were subcloned to a PiggyBac vector. The fragment encoding RapR-Src-as2-mCherry-myc was amplified by PCR from pUSE-RapR-Src-as2-mCherry-myc by using the primer 5' – ATG CAG CTA GCA TCA TGG GCA GCA ACA AGA GC – 3' (BmtI coding strand) and 5' – ATG CAT CTA GAA TCA CCA GTT TCT TCC GGA CTT GTA C – 3' (XbaI non-coding strand). This fragment was inserted at the BmtI and XbaI site in the PiggyBac vector. The fragment encoding ipep-FRB* was amplified by PCR from pUSE-ipep-FRB* by using the

primer 5' - GCG GCG CCC TGC CCG TCC CAC CAG GTG AGT TCC GCG TTA CAT AAC TTA CGG – 3' (SexAI, coding strand), and 5' – GGC CGG TTA CCG CCT GTT GAC CTG GTC GCG TTA AGA TAC ATT GAT GAG TTT GGA C – 3' (SexAI, non-coding strand). This fragment was inserted at the SexAI site in pPBH-TREtight-RapR-Src-as2-mCherry-myc using In-Fusion® Cloning Kit.

3.2.2.3 Biosensor validation - fluorometry assay

pTriEX- Ypet-PBD-$(ER/K)_n$-mCerulean-Rac1 and pTriEX4-mTFP1/cp227-PBD-$(ER/K)_n$-Venus/cp229-Rac1 (n = 10nm, 20nm, or 30 nm) biosensor constructs were co-transfected with upstream regulators (Tiam1 or GDI) into 293T cells plated $1x10^5$ per well overnight in 6-well plates, using Lipofectamine 3000 (Invitrogen) according to the manufacture's protocols. The total amount of DNA was 750 ng per well (150 ng of the biosensor and 600 ng of the regulator). At 48h after transfection, cells were detached with brief trypsin treatment and were resuspended in 500 μL of ice-cold PBS. Cell suspensions were transferred into a quartz cuvette. Their fluorescent spectrum was then recorded by a fluorometer. The FP biosensors and cpFP biosensors were excited at 433 nm and 460 nm respectively. Their emission spectra were recorded from 450 to 600 nm and 480 to 600 nm respectively. Spectra were background-subtracted with spectra of non-transfected cells and normalized according to their spectrum integral.

3.2.2.4 Multi-well plate assays

Biosensor validation – multi-well plate assays with permeabilized mammalian cells. To validate the LRET biosensors, pTriEX4-EGFP-PBD-$(ER/K)_n$-eDHFR-Rac1 (n = 10nm, 20nm, or 30 nm) biosensor constructs were co-transfected with upstream regulators (Tiam1 or GDI) into 293T cells using Lipofectamine 2000. One day

prior to transfection, cells were seeded at 9000 cells per well in a poly-L-lysine coated 96-well plate. The amount of DNA per well was 4.25 ng of the biosensor and 17 ng of the regulator. After 48h, growth media in the wells were discarded carefully and 70 uL of lysis buffer with TMP-cs124-TTHA (25 nM) was added into the wells. The plate was kept at room temperature in dark for 10 min prior to the first measurement. Background control wells received the same transfection media but no biosensor construct and the same lysis buffer with Tb(III) complex. The emission signals were background-subtracted and FRET/acceptor and FRET/ donor emission ratios were calculated.

Inhibition assay with permeabilized mammalian cells. pTriEX4-EGFP-PBD-$(ER/K)_{30}$-eDHFR-Rac1 biosensor construct were co-transfected with upstream regulators (Tiam1 or GDI) into 293T cells using Lipofectamine 2000. One day prior to transfection, cells were seeded at 9000 cells per well in a poly-L-lysine coated 96-well plate. The amount of DNA per well was 4.25 ng of the biosensor and 17 ng of the regulator. After 24h, cells were incubated with 100 uL of growth media containing NSC23766 or EHT1864 inhibitor (final concentration 50 uM) for 4 hours or overnight. Negative control wells received growth media without the inhibitor. Next, growth media in the wells were discarded carefully and 70 uL of lysis buffer with TMP-cs124-TTHA (25 nM) was added into the wells. The plates were kept at room temperature in dark for 10 min prior to the first measurement. Background control wells received the same transfection media but no biosensor construct and were treated the same as sample wells for the rest of the experiment. The emission signals were background-subtracted and FRET/acceptor and FRET/ donor emission ratios were calculated.

3.2.2.5 Stable expression of biosensor plasmids

Rac1 biosensor constructs in PiggyBac vector system were transfected into MEF cells using Lipofectamine 2000. Hygromycin selection was applied to generate the stable cell lines. The cells were then FACS sorted to obtain a population of uniform but medium biosensor expression levels. For imaging experiments, cells were induced by adding 100 ng/mL doxycycline and appropriate biosensor expression levels were achieved at 24h following the induction.

3.2.2.6 Cell Imaging and Image Processing

Cell imaging of cpFP Rac1 biosensor. HeLa cells stably expressing RapR-Src-as2-mcherry and ipep-FRB were plated on a fibronectin-coated 25 mm–diameter glass coverslip by placing the coverslip inside a well of a 6-well plate and adding 35,000 cells/well. Cells were incubated for 2–4 h. Before imaging, coverslips were placed into an Attufluor Cell Chamber (Invitrogen, catalog no. A78-16) with Ham's f12 K medium (no red) containing 10mM HEPES, DL lactate, and Oxy Fluor, supplemented with 1% (vol/vol) FBS. Live-cell imaging was done using an Olympus IX-83 microscope controlled by Metamorph software and equipped with a heated stage (Warner Instruments), Olympus UPlanSAPO 40× (oil, N.A. 1.25) objective, Xcite 120 LED (Lumen Dynamics) light source, and Image EMX2 CCD (Hamamatsu) camera. We thank Dr. Andrei Karginov at Department of Pharmacology, UIC for helping and providing the equipment for this experiment.

Cell imaging of LRET Rac1 biosensor. Time-gated luminescence images were acquired using a previously described epi-fluorescence microscope (Axiovert 200, Carl Zeiss, Inc.).[70, 71] For each time-gated image acquisition, the signal from multiple

excitation/emission events was accumulated on the ICCD sensor and read out at the end of the camera frame. The UV LED pulse width and pulse period, the intensifier delay time and on-time, the camera frame length (66.67 ms – 2 s) and the intensifier gain voltage could be varied independently. The source/camera timing parameters were the same for all of the time-resolved images and data presented here: excitation pulse width, 1500 μs, pulse period, 3000 μs, delay time, 10 μs, intensifier on-time, 1480 μs. All data reported here was acquired at a gain of 833 V. The camera control software enabled summation of multiple frames to yield a single composite. TIFF image with a bit depth equal to 1024 multiplied by the number of frames. All images reported here were summations of four frames (bit depth, 4096), and a feature of the camera control software was enabled that removes large variations in signal resulting from ion-feedback noise of the intensifier.

Image Processing. Raw images were imported into NIH ImageJ (v1.42q) for all processing operations including cropping, contrast adjustment, and quantitative analysis.[72] For each channel, 20 dark frames and 20 bright field images were stacked, converted to 32 bits, and median-filtered (radius 1), and each stack was averaged. The flat-field average was divided by the mean intensity of its central nine pixels to generate a normalized flat-field image. For each sample image, a median filter (radius 1) was applied and the master dark frame was subtracted. The resulting image was then divided by the normalized, master flat-field image, and the mean value of the detector offset was added back to the image. For ratiometric images and measurements, a binary mask was created by first averaging a series of Ypet images and then applying a threshold to highlight only regions exhibiting signal. The mask was applied to background-subtracted

the FRET images were then divided by the donor image. Intensity-modulated ratiometric displays were generated using the Fire lookup table in ImageJ and a color lookup table was applied.

3.3 Results and Discussion

3.3.1 Biosensor designs

In general, our sensor structure consists of the following (N to C): an FP, a p21 binding domain (PBD), an ER/K linker, a second FP or eDHFR for Tb(III) probe labeling, and a full-length Rac1 (Figure 14A). Rac1 was placed at the carboxy terminus of the biosensor to maintain the correct regulatory cycle of Rac1 by RhoGDI. To identify a Rac1 biosensor with the best performance and to characterize the versatility of the LRET biosensor toolkit, we built a series of nine Rac1 biosensors by combining three ER/K linkers of various length (10 nm, 20 nm, or 30 nm) and three FRET donor/acceptor pairs (mCerulean/Ypet, circularly permutated mTFP1/circularly permutated Venus, Tb(III) probe/EGFP) (Figure 14B). As discussed in chapter 2, the rigidity of ER/K linkers helps reduce background FRET, while random break can be induced to promote protein interactions. The three FRET pairs were chosen because mCerulean/YPet is one of the most preferred FP pairs for FRET investigations; the circular permutation of mTFP1 (cp227)/Venus (cp229) was previously used in the Rac1-2G biosensor,[47] which had the best spectral property among Rac1 biosensors made by cp variants of mTFP1 and Venus; Tb complex/EGFP is our LRET pair. In the LRET biosensors, a TMP-Tb(III) complex heterodimer (Figure 10) enters cells via cell-penetrating peptide and binds to eDHFR in the biosensor construct, completing the sensor.

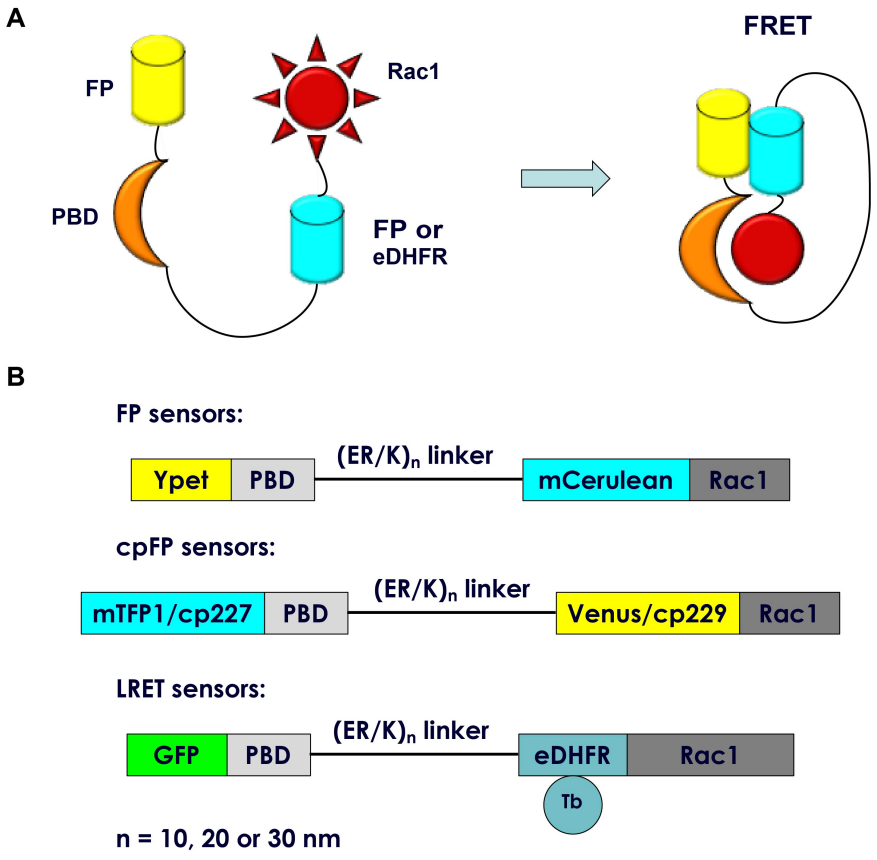

Figure 14. Designation of FRET and LRET Rac1 biosensors. (A) Schematic representation and (B) mammalian expression construct of single-chain FRET Rac1 biosensors. A series of nine sensors was constructed in which alpha-helical ER/K linkers of different (10 nm, 20 nm and 30 nm) length were combined with three fluorophore pairs: mCerulean/Ypet, circularly permutated mutant (cp227) of mTFP1/circularly permutated mutant (cp229) of Venus, and Tb complex/EGFP. (C) Sequence of a 30 nm alpha-helical ER/K linker. The linker is rigid to keep protein components far apart in OFF state and can induce sudden break to promote protein interaction in ON state of the biosensors.

3.3.2 Biosensor characterization

All nine biosensors were characterized for their dynamic range by co-expressing the sensors with Rac1 upstream regulators and using a fluorometer (for FP or cpFP biosensors) or a plate reader (for LRET biosensors) to read out emission signals. Tiam1 was used to keep the sensors in their activation state while GDI did the opposite. In the fluorometry assay, 293T cells co-expressing both the biosensor and Tiam1 or GDI were scanned for emission profiles at the donor excitation wavelengths. The assay was done in cell suspension using a cuvette-based fluorometer. As for plate reader assay, 293T cells co-expressing the biosensor and Tiam1 or GDI were seeded in a 96 well plate. A lysis solution containing TMP-TTHA-cs124 (Figure 10) was added to the cells 10 min before measuring maximum donor and FRET emissions. Dynamic range of each biosensor was calculated as $(R_a-R_i)/R_i$ or $\Delta R/R_i$ where R_a and R_i were FRET/donor emission ratio at active and inactive states, respectively. The reported Rac1-2G biosensor, comprising of mTFP1(cp227), PBD, a flexible linker, Venus(cp229), and Rac1 from N to C, was used as a control for the characterization method.

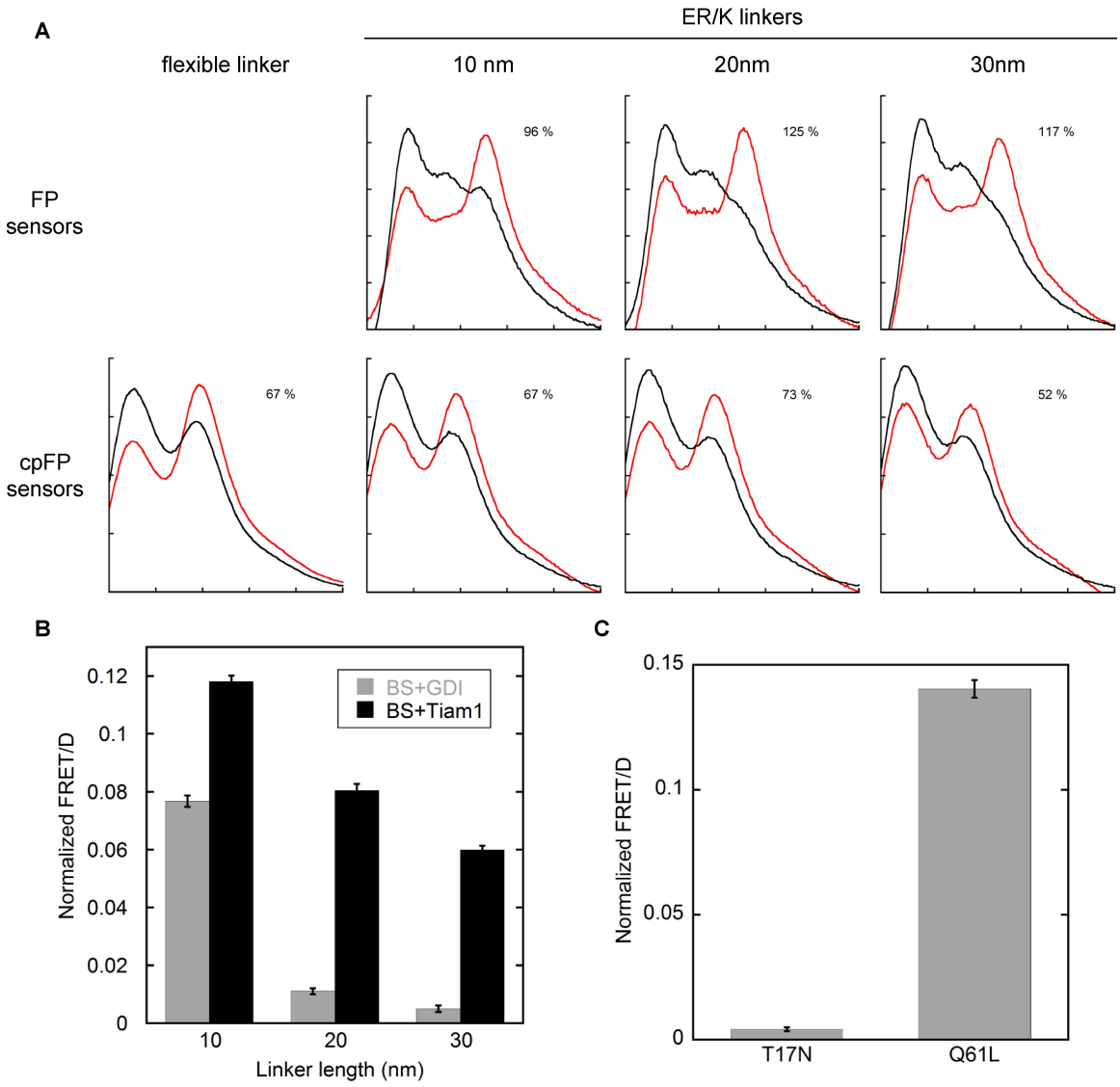

Figure 15. Evaluation of Rac1 biosensors by fluorometry and plate reader assay. Rac1 biosensors were evaluated by co-expressed the sensor with Tiam1 (On state-red trace in A or black bar in B) or RhoGDI (Off state-black trace in A or gray bar in B) in 293T cells. (A) Cells co-expressing FP or cpFP sensors and the regulators were scanned for emission profiles in cell suspension using a cuvette-based fluorometer. $\Delta R/R_i$ values representing differences in FRET efficiency between the On and Off states are shown for the indicated biosensor. (B) Cells co-expressing LRET biosensors and the regulators were grown in a 96-well plate. Following overnight incubation, cells were treated with lysis buffer containing TMP-TTHA-cs124 (25 nM). The time-gated emission (gate delay, 0.2 ms) at 520 nm (Tb-to-GFP FRET) and 620 nm (Tb only) were measured using a time-resolved fluorescence plate reader. Substantial larger FRET/Tb ratios were observed in the positive control wells (Tiam1) relative to those seen in the negative controls (RhoGDI). (C) 293T cells expressing inactive (Rac1 T17N) or active (Rac1 Q61L) mutants of the LRET biosensor with 30 nm ER/K linker were grown in a 96-well plate and underwent the same lysis-buffer treatment and plate-reader measurement as in B.

Among nine biosensors, LRET biosensors showed outstanding dynamic ranges, while FP or cpFP biosensors possessed low to-medium dynamic ranges. Specifically, LRET sensors with 10 nm, 20 nm, or 30 nm linkers exhibited maximum differences in $\Delta R/R_i$ values 50%, 600%, and 1100%, respectively (Figure 15B). To further validate this result, we performed the same plate reader assay on cells expressing active (Rac1 T17N) or inactive (Rac1 Q61L) mutants of the LRET sensor with the 30 nm linker. The difference in the emission ratio of these two mutants agreed with that of Tiam1/GDI assay (Figure 15C).

The unique properties of the Tb(III) complex as a donor can explain the robust dynamic range of LRET sensors. In essence, the narrow emission bands of the Tb complex minimize bleedthrough, and the TGL detection of long-lived donor and FRET signals eliminates background fluorescence. Therefore, even without purifying proteins after lysing cells, our plate reader assay still gave distinct signals between two states of the biosensors. On the other hand, the low protein concentration in a plate well is far bellowed the detection limit of FP or cpFP biosensors. Consequently, fluorometry assays were used to characterize these types of sensors instead of plate reader assays. For both FP and cpFP biosensors, the highest dynamic ranges (125% and 73% respectively) were observed in the sensor with 20 nm ER/K linker (Figure 15A). Also, the $\Delta R/R_i$ value of the control (Rac1-2G) was consistent with the reported data, indicating the validation of the characterization method.

In general, all biosensors experienced an increase in dynamic range with the rise of ER/K linker length. The characterization data illustrated that longer linkers significantly decreased background FRET (second peak of the black trace in Figure 15A

or gray bar in figure 15B) while slightly reducing On-state FRET (second peak of the red trace in figure 15A or black bar in figure 15B). As a result, sensors with the 20 nm or 30 nm linker usually had the best performance. The effect of ER/K linkers on the sensor properties can be understood by considering its conformational behavior. While the fully random-coil structure of flexible middle linkers, commonly used in biosensors, allows many different conformations in the unbound state, causing an excessive basal FRET, alpha-helical ER/K linkers predominantly adopt an extended conformation in the unbound state. This rigid structure also explains why the longer the ER/K linker is, the lower the Off-state FRET. Furthermore, ER/K linkers are assumed to undergo rare stochastic breaks that enable protein interactions following activation. Although the frequency of these breaks increases linearly with increasing ER/K alpha helix length, the probability of end-to-end interaction decreases due to the lack of spatial coordination between the breaks. This reduction leads to a decrease in the effective concentration of interacting proteins that necessarily reduces the proportion of sensors in the bound or On-state and leads to a slight decline in FRET.

ER/K linkers substantially impacted the performance of LRET Rac1 biosensors while marginally improving that of FP, especially cpFP biosensors. The strong influence in LRET biosensors may be due to the long distance of LRET, which causes high baseline signals and requires a long rigid linker for extended conformation in the Off state. Second, orientation factors are essential in FRET efficiency between FPs, especially cpFPs. In fact, the purpose of using cpFPs is to alter the arrangement of protein elements in the sensors so as to produce favorable spatial orientation (κ^2). Thus, the rigidity of ER/K linkers may counteract this purpose by restricting the mobility of cpFP

dipole toward unfavorable (κ^2 <2/3) orientation. In general, a flexible linker is preferred in FP and cpFP sensors because it provides little, if any, restriction on the tumbling and twisting of the fluorophores. In contrast, LRET does not depend on the dipole orientation of the donor or acceptor, as mentioned in chapter 2. Hence, the use of a rigid linker does not introduce any downside on orientation factors.

3.3.3 Biosensors in live cells

We next examined the spatial and temporal resolution of our sensors in HeLa cells migrating on fibronectin. Based on the characterization result, we chose to carry out live-cell microscopy on the FP and LRET biosensor with 20 nm and 30 nm ER/K linkers, respectively. In general, activation of Rac1 may be induced by incubating cells with growth factors (EGF, PDGF) or other extracellular stimuli. However, this approach triggers a multitude of parallel signaling pathways and often a brief, transient activation of Rac1 which significantly complicates the analysis of sensor activity. Therefore, we applied a recently developed protein engineering method that employed a rapamycin-regulated allosteric switch to regulate tyrosine kinase c-Src (Src) activation.[100] In this way, activation of Rac1 could be controlled indirectly by rapamycin-induced Src activation. For live-cell imaging, cells co-expressing the biosensor and Src constructs were seeded on a fibronectin-coated chamber slide. Cells were imaged every 2 min for 20 min before and 40 min after adding rapamycin.

As for the FP sensor with 20 nm ER/K linker, robust Rac1 activation near protruding edges of stimulated cells was observed following rapamycin addition. Cells started vigorous spreading and protrusion a few minutes after rapamycin addition.

Activation of the sensor was consistently observed wherever protrusions were extending (Figure 16A).

Cells coexpressing the LRET sensor with 30 nm ER/K linker and Src constructs were incubated in culture medium containing 12 μM of the cell-permeable TMP-Lumi4-R_9 at room temperature. After 15 min, cells were washed two times with PBS, immersed in imaging medium and then imaged immediately. Continuous-wave images of GFP fluorescence revealed the distribution of single-chain biosensors throughout the cytoplasm. Time-gated images of Tb(III) luminescence and Tb(III)-to-GFP sensitized emission showed Tb(III) probe delivery throughout the cytoplasm and nucleus (Figure 16B). Further studies to evaluate the LRET Rac1 sensor for live cell imaging will require the use of an automated LRET microscope. Construction of this instrument was not yet complete at the time this dissertation was written.

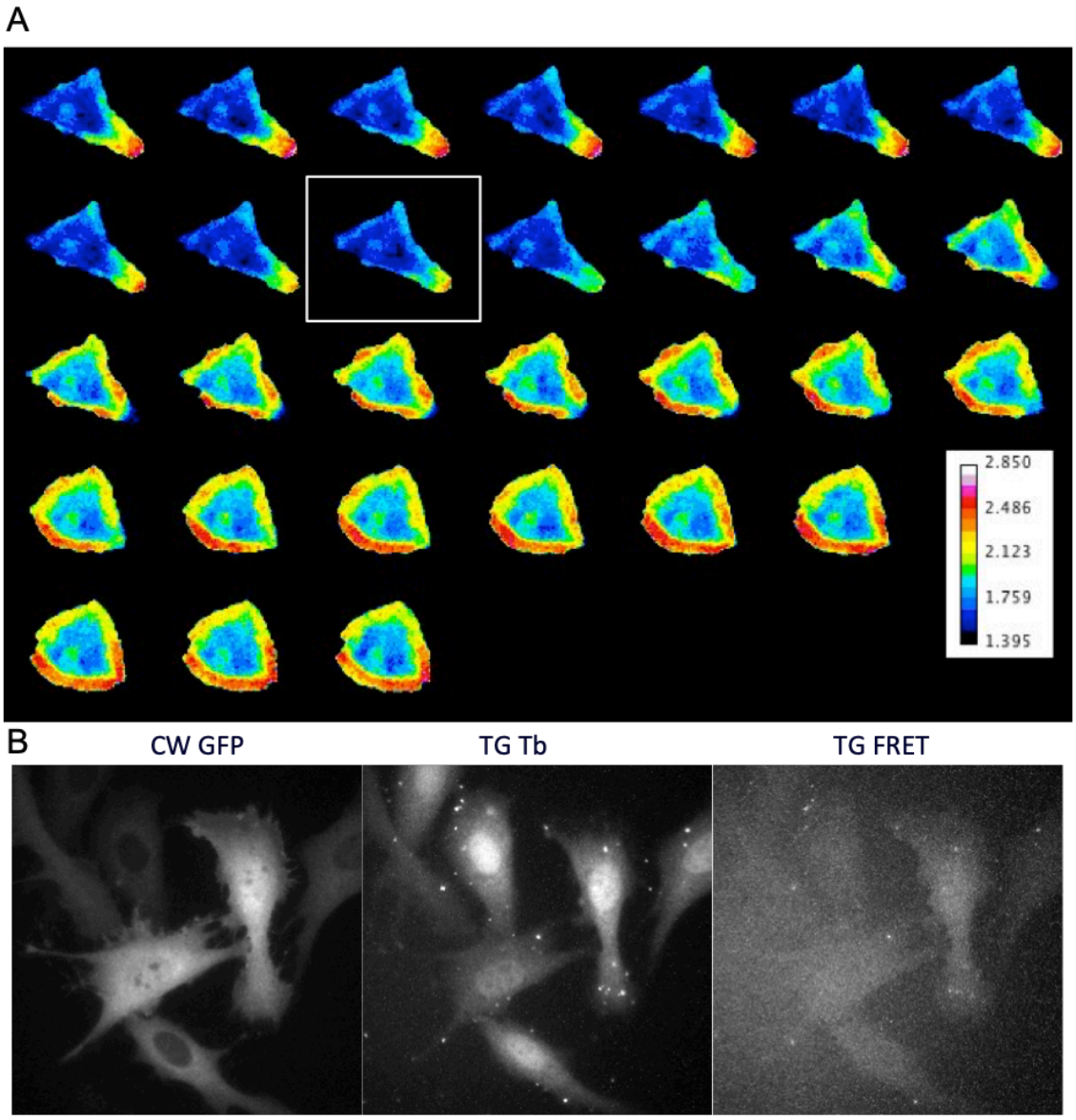

Figure 16. Live-cell imaging of Rac1 biosensors. (A) A HeLa cell co-expressing the FP Rac1 sensor with the 20 nm ER/K linker (transient transfection) and Src constructs (stably transfection) was imaged for every 2 min in 1 hour. Rapamycin (500 nM) was added after 20 min (indicated by the square). The montage shows FRET/mCerulean ratio images of the biosensor in a living cell. Warmer colors reflect higher local activity of Rac1. (B) Time-gated luminescence microscopy of cells stably expressing the LRET Rac1 sensor with the 30 nm ER/K linker. Micrographs: CW, steady-state fluorescence (λ_{ex} 480 nm, λ_{em} 535 nm); Tb(III), time-gated Tb(III) luminescence (λ_{ex} 365 nm, λ_{em} 620 nm, gate delay 10 μs); FRET, time-gated Tb(III)-to-GFP sensitized emission (λ_{ex} 365 nm, λ_{em} 520 nm, gate delay 10 μs).

3.3.4 Inhibitor assay

Increasing evidence supports the involvement of Rac1 signaling alterations in cancers.[90, 101] Because mutations in Rac1 proteins are sporadic, the mechanism of Rac1 in cancer likely occurs through its overexpression or hyperactivity.[102] Accordingly, the inhibition of Rac1 is speculated to have an antiproliferative effect on cancer cells.[101] Several small molecules have been identified as Rac1 inhibitors through virtual screening of chemical libraries followed by *in vitro* characterization of hits. NSC23766 and EHT 1864 were among the first developed Rac1 inhibitors with the capability to discern from other Rho family GTPases, such as Cdc42 or RhoA.[94, 95] The former impedes Rac1 activation by occupying the binding location of two Rac1 GEFs: Trio and Tiam1,[94] while the latter keeps Rac1 in an inactive state and prevents its binding to downstream effector.[95]

Here, we sought to assess the potential of our LRET Rac1 biosensor with 30 nm ER/K linker in the detection and quantification of Rac1 inhibition in a multi-well plate format with permeabilized cells. We measured the effects of NSC23766 and EHT 1864 as inhibitors of Rac1 activation. 293T cells were seeded into 96-well plates (9000 cells/well), followed by transient transfection of the biosensor and Tiam1 on the next day. Tiam1 was overexpressed in cells to activate Rac1, mimicking the deregulation of this regulator in cancer cells.[103] 48h after transfection, cells were incubated with growth media containing the inhibitor (50 uM) for four hours or overnight. After removing the growth media, a lysis buffer containing TMP-Lumi4-Tb (25 nM) was added to the wells, and the plate was incubated at room temperature for 10 min. Negative control wells went through the same treatment but without the addition of the inhibitor. Following

incubation, the time-gated Tb(III)-to-GFP and Tb(III) emission signals were measured at 520 nm and 615 nm, respectively. The 520 nm signal from each well was divided by the 615 nm signal to minimize well-to-well variability resulting from differences in probe amounts or sample absorbance. Then, the mean 520/615 emission ratio from 12 control wells containing non-expressing cells and lysis buffer solution (25 nM TMP-Lumi4-Tb, no rapamycin) was subtracted from each sample well to yield a background-corrected, LRET/Tb ratio.

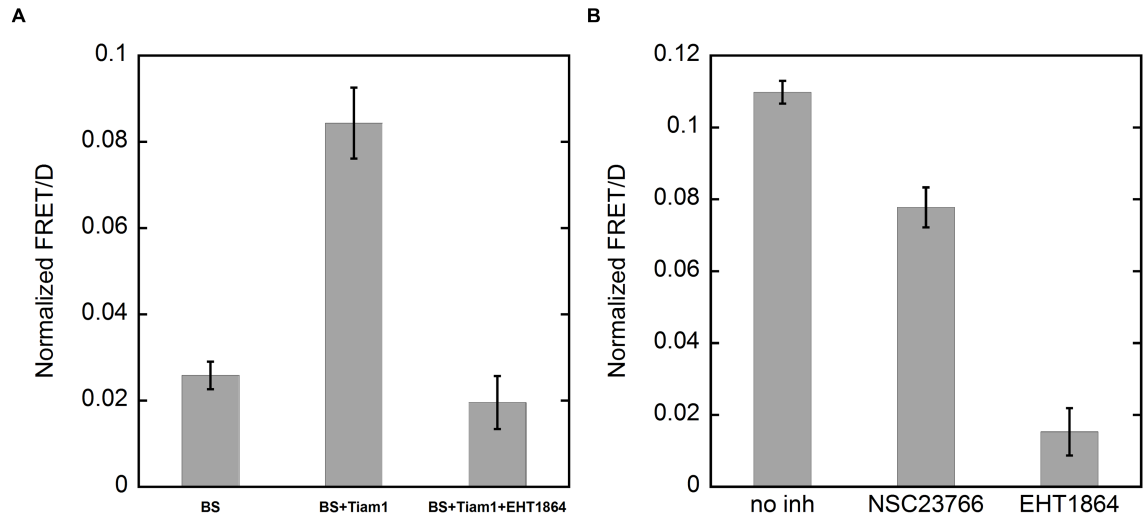

Figure 17. Large reductions were observed in multi-well plate when NSC23766 and EHT 1864 inhibit Rac1 activation. A. 293T cells expressing the sensor alone (BS) or with Tiam1 (BS+Tiam1) were grown in 96-well. Time-gated measurements were obtained following 4h incubation with EHT 1864 and addition of a lysis buffer containing TMP-TTHA-cs124. B. 293T cells co-expressing the sensor and Tiam1 were grown in 96-well overnight with or without inhibitors in the media. Time-gated measurements were taken after adding the lysis buffer as in A.

The LRET Rac1 biosensor with 30 nm ER/K linker robustly responded to Rac1 inhibitors in the 96-well plate assay. After four-hour incubation, full inhibition with 50 uM EHT 1864 yielded LRET/Tb signal decrease of more than 70%. The ratio went down to the same level as the biosensor without Tiam1 activation (Figure 17A). Compared to EHT1864, NSC23766 partially inhibited the Rac1 activity after an overnight incubation (Figure 17B). Z' factor values were calculated to determine data quality. Inhibition assays with overnight incubation of EHT 1864 or NSC23766 possessed Z' factor values of 0.69 and 0.19, respectively.

3.4 Conclusion

The data obtained with the Rac1 model system confirm the strong potential of LRET biosensors for both live-cell imaging and cell-based screening of PPIs. Extraordinary dynamic range stems from time-gated detection of LRET that eliminates non-specific fluorescent background and from the incorporation of ER/K linkers that maintains the donor and acceptor far apart in the open sensor configuration. These features enable robust detection of Rac1 activation or inhibition in cell lysates in 96-well plates and promise dynamic visualization of cells expressing the sensor with TGL microscopy. ER/K linkers, while having a marginal effect on the dynamic range of FP or cp-FP Rac1 biosensors, effectively increase the sensitivity of LRET biosensors. In principle, LRET Rac1 biosensors should support medium or high throughput detection of small molecules inhibitor for Rac1 or any other proteins, especially proteins that are difficult to purify or isolate from intact environment. Moreover, Tb(III) can sensitize differently colored acceptors, offering the potential for multiplexed imaging or analysis.

Taken together, the results presented here show that the LRET biosensor toolkit is versatile when used to improve existing biosensor templates.

REFERENCES

[1] Kholodenko, B. N. (2006) Cell-signalling dynamics in time and space, *Nat Rev Mol Cell Biol 7*, 165-176.

[2] Pawson, T., and Nash, P. (2003) Assembly of cell regulatory systems through protein interaction domains, *Science 300*, 445-452.

[3] Ryan, D. P., and Matthews, J. M. (2005) Protein-protein interactions in human disease, *Curr Opin Struct Biol 15*, 441-446.

[4] Welch, C. M., Elliott, H., Danuser, G., and Hahn, K. M. (2011) Imaging the coordination of multiple signalling activities in living cells, *Nat Rev Mol Cell Bio 12*, 749-756.

[5] Specht, E. A., Braselmann, E., and Palmer, A. E. (2017) A Critical and Comparative Review of Fluorescent Tools for Live-Cell Imaging, *Annu Rev Physiol 79*, 93-117.

[6] Piston, D. W., and Kremers, G. J. (2007) Fluorescent protein FRET: the good, the bad and the ugly, *Trends Biochem Sci 32*, 407-414.

[7] Pertz, O., Hodgson, L., Klemke, R. L., and Hahn, K. M. (2006) Spatiotemporal dynamics of RhoA activity in migrating cells, *Nature 440*, 1069-1072.

[8] Taylor, D. L., and Wang, Y. L. (1980) Fluorescently Labeled Molecules as Probes of the Structure and Function of Living Cells, *Nature 284*, 405-410.

[9] Toseland, C. P. (2013) Fluorescent labeling and modification of proteins, *J Chem Biol 6*, 85-95.

[10] Tsien, R. Y. (1998) The green fluorescent protein, *Annual Review of Biochemistry 67*, 509-544.

[11] Zhang, J., Campbell, R. E., Ting, A. Y., and Tsien, R. Y. (2002) Creating new fluorescent probes for cell biology, *Nat Rev Mol Cell Biol 3*, 906-918.

[12] Miyawaki, A., and Niino, Y. (2015) Molecular spies for bioimaging--fluorescent protein-based probes, *Mol Cell 58*, 632-643.

[13] Ni, Q., Mehta, S., and Zhang, J. (2018) Live-cell imaging of cell signaling using genetically encoded fluorescent reporters, *Febs J 285*, 203-219.

[14] Ormo, M., Cubitt, A. B., Kallio, K., Gross, L. A., Tsien, R. Y., and Remington, S. J. (1996) Crystal structure of the Aequorea victoria green fluorescent protein, *Science 273*, 1392-1395.

[15] Rodriguez, E. A., Campbell, R. E., Lin, J. Y., Lin, M. Z., Miyawaki, A., Palmer, A. E., Shu, X., Zhang, J., and Tsien, R. Y. (2017) The Growing and Glowing Toolbox of Fluorescent and Photoactive Proteins, *Trends Biochem Sci 42*, 111-129.

[16] Grynkiewicz, G., Poenie, M., and Tsien, R. Y. (1985) A new generation of Ca2+ indicators with greatly improved fluorescence properties, *J Biol Chem 260*, 3440-3450.

[17] Magliery, T. J., Wilson, C. G., Pan, W., Mishler, D., Ghosh, I., Hamilton, A. D., and Regan, L. (2005) Detecting protein-protein interactions with a green fluorescent protein fragment reassembly trap: scope and mechanism, *J Am Chem Soc 127*, 146-157.

[18] Miesenbock, G., De Angelis, D. A., and Rothman, J. E. (1998) Visualizing secretion and synaptic transmission with pH-sensitive green fluorescent proteins, *Nature 394*, 192-195.

[19] Baird, G. S., Zacharias, D. A., and Tsien, R. Y. (1999) Circular permutation and receptor insertion within green fluorescent proteins, *P Natl Acad Sci USA 96*, 11241-11246.

[20] Nakai, J., Ohkura, M., and Imoto, K. (2001) A high signal-to-noise Ca(2+) probe composed of a single green fluorescent protein, *Nat Biotechnol 19*, 137-141.

[21] Campbell, R. E. (2009) Fluorescent-Protein-Based Biosensors: Modulation of Energy Transfer as a Design Principle, *Anal Chem 81*, 5972-5979.

[22] Jares-Erijman, E. A., and Jovin, T. M. (2003) FRET imaging, *Nat Biotechnol 21*, 1387-1395.

[23] van Dongen, E. M., Evers, T. H., Dekkers, L. M., Meijer, E. W., Klomp, L. W., and Merkx, M. (2007) Variation of linker length in ratiometric fluorescent sensor proteins allows rational tuning of Zn(II) affinity in the picomolar to femtomolar range, *J Am Chem Soc 129*, 3494-3495.

[24] Nguyen, A. W., and Daugherty, P. S. (2005) Evolutionary optimization of fluorescent proteins for intracellular FRET, *Nat Biotechnol 23*, 355-360.

[25] Ohashi, T., Galiacy, S. D., Briscoe, G., and Erickson, H. P. (2007) An experimental study of GFP-based FRET, with application to intrinsically unstructured proteins, *Protein Sci 16*, 1429-1438.

[26] Vinkenborg, J. L., Evers, T. H., Reulen, S. W., Meijer, E. W., and Merkx, M. (2007) Enhanced sensitivity of FRET-based protease sensors by redesign of the GFP dimerization interface, *Chembiochem 8*, 1119-1121.

[27] Fuller, B. G., Lampson, M. A., Foley, E. A., Rosasco-Nitcher, S., Le, K. V., Tobelmann, P., Brautigan, D. L., Stukenberg, P. T., and Kapoor, T. M. (2008) Midzone activation of aurora B in anaphase produces an intracellular phosphorylation gradient, *Nature 453*, 1132-1136.

[28] Cristobal G. dos Remedios, P. D. J. M. (1995) Fluorescence resonance energy transfer spectroscopy is a reliable "ruler" for measuring structural changes in proteins. Dispelling the problem of the unknown orientation factor, *J Struct Biol 115*, 175-185.

[29] Deuschle, K., Okumoto, S., Fehr, M., Looger, L. L., Kozhukh, L., and Frommer, W. B. (2005) Construction and optimization of a family of genetically encoded metabolite sensors by semirational protein engineering, *Protein Sci 14*, 2304-2314.

[30] Nagai, T., Yamada, S., Tominaga, T., Ichikawa, M., and Miyawaki, A. (2004) Expanded dynamic range of fluorescent indicators for Ca(2+) by circularly permuted yellow fluorescent proteins, *Proc Natl Acad Sci U S A 101*, 10554-10559.

[31] Patterson, G. H., Piston, D. W., and Barisas, B. G. (2000) Forster distances between green fluorescent protein pairs, *Anal Biochem 284*, 438-440.

[32] David A. Zacharias, J. D. V., Alexandra C. Newton, Roger Y. Tsien. (2002) Partitioning of lipid-modified monomeric GFPs into membrane microdomains of live cells, *Science 296*, 913-916.

[33] Miyawaki, A. (2011) Development of probes for cellular functions using fluorescent proteins and fluorescence resonance energy transfer, *Annu Rev Biochem 80*, 357-373.

[34] Vogel, S. S., Thaler, C., and Koushik, S. V. (2006) Fanciful FRET, *Sci STKE 2006*, re2.

[35] Sun, Y., Day, R. N., and Periasamy, A. (2011) Investigating protein-protein interactions in living cells using fluorescence lifetime imaging microscopy, *Nat Protoc 6*, 1324-1340.

[36] Elder, A. D., Domin, A., Kaminski Schierle, G. S., Lindon, C., Pines, J., Esposito, A., and Kaminski, C. F. (2008) A quantitative protocol for dynamic measurements of protein interactions by Förster resonance energy transfer-sensitized fluorescence emission, *Journal of The Royal Society Interface 6*.

[37] Gadella, T. W. J. (2009) *FRET and FLIM techniques*, 1st ed., Elsevier, Amsterdam ; Boston.

[38] Rajendran, M., Yapici, E., and Miller, L. W. (2014) Lanthanide-based imaging of protein-protein interactions in live cells, *Inorg Chem 53*, 1839-1853.

[39] You, X., Nguyen, A. W., Jabaiah, A., Sheff, M. A., Thorn, K. S., and Daugherty, P. S. (2006) Intracellular protein interaction mapping with FRET hybrids, *Proc Natl Acad Sci U S A 103*, 18458-18463.

[40] Lam, A. J., St-Pierre, F., Gong, Y., Marshall, J. D., Cranfill, P. J., Baird, M. A., McKeown, M. R., Wiedenmann, J., Davidson, M. W., Schnitzer, M. J., Tsien, R. Y., and Lin, M. Z. (2012) Improving FRET dynamic range with bright green and red fluorescent proteins, *Nat Methods 9*, 1005-1012.

[41] Kraynov, V. S., Chamberlain, C., Bokoch, G. M., Schwartz, M. A., Slabaugh, S., and Hahn, K. M. (2000) Localized Rac activation dynamics visualized in living cells, *Science 290*, 333-337.

[42] Machacek, M., Hodgson, L., Welch, C., Elliott, H., Pertz, O., Nalbant, P., Abell, A., Johnson, G. L., Hahn, K. M., and Danuser, G. (2009) Coordination of Rho GTPase activities during cell protrusion, *Nature 461*, 99-103.

[43] Itoh, R. E., Kurokawa, K., Ohba, Y., Yoshizaki, H., Mochizuki, N., and Matsuda, M. (2002) Activation of rac and cdc42 video imaged by fluorescent resonance energy transfer-based single-molecule probes in the membrane of living cells, *Mol Cell Biol 22*, 6582-6591.

[44] Komatsu, N., Aoki, K., Yamada, M., Yukinaga, H., Fujita, Y., Kamioka, Y., and Matsuda, M. (2011) Development of an optimized backbone of FRET biosensors for kinases and GTPases, *Mol Biol Cell 22*, 4647-4656.

[45] Moshfegh, Y., Bravo-Cordero, J. J., Miskolci, V., Condeelis, J., and Hodgson, L. (2014) A Trio-Rac1-Pak1 signalling axis drives invadopodia disassembly, *Nat Cell Biol 16*, 574-586.

[46] Miskolci, V., Wu, B., Moshfegh, Y., Cox, D., and Hodgson, L. (2016) Optical Tools To Study the Isoform-Specific Roles of Small GTPases in Immune Cells, *J Immunol 196*, 3479-3493.

[47] Fritz, R. D., Menshykau, D., Martin, K., Reimann, A., Pontelli, V., and Pertz, O. (2015) SrGAP2-Dependent Integration of Membrane Geometry and Slit-Robo-Repulsive Cues Regulates Fibroblast Contact Inhibition of Locomotion, *Dev Cell 35*, 78-92.

[48] Iversen, P. W., Eastwood, B. J., Sittampalam, G. S., and Cox, K. L. (2006) A comparison of assay performance measures in screening assays: signal window, Z' factor, and assay variability ratio, *Journal of biomolecular screening 11*, 247-252.

[49] Herce, H. D., Deng, W., Helma, J., Leonhardt, H., and Cardoso, M. C. (2013) Visualization and targeted disruption of protein interactions in living cells, *Nat Commun 4*, 2660.

[50] Lundholt, B. K., Heydorn, A., Bjorn, S. P., and Praestegaard, M. (2006) A simple cell-based HTS assay system to screen for inhibitors of p53-Hdm2 protein-protein interactions, *Assay Drug Dev Technol 4*, 679-688.

[51] Michnick, S. W., Ear, P. H., Manderson, E. N., Remy, I., and Stefan, E. (2007) Universal strategies in research and drug discovery based on protein-fragment complementation assays, *Nat Rev Drug Discov 6*, 569-582.

[52] Eyckerman, S., Lemmens, I., Catteeuw, D., Verhee, A., Vandekerckhove, J., Lievens, S., and Tavernier, J. (2005) Reverse MAPPIT: screening for protein-protein interaction modifiers in mammalian cells, *Nat Methods 2*, 427-433.

[53] Petschnigg, J., Groisman, B., Kotlyar, M., Taipale, M., Zheng, Y., Kurat, C. F., Sayad, A., Sierra, J. R., Mattiazzi Usaj, M., Snider, J., Nachman, A., Krykbaeva, I., Tsao, M. S., Moffat, J., Pawson, T., Lindquist, S., Jurisica, I., and Stagljar, I. (2014) The mammalian-membrane two-hybrid assay (MaMTH) for probing membrane-protein interactions in human cells, *Nat Methods 11*, 585-592.

[54] Pfleger, K. D., and Eidne, K. A. (2006) Illuminating insights into protein-protein interactions using bioluminescence resonance energy transfer (BRET), *Nat Methods 3*, 165-174.

[55] Song, Y., Madahar, V., and Liao, J. (2011) Development of FRET Assay into Quantitative and High-throughput Screening Technology Platforms for Protein-Protein Interactions, *Ann Biomed Eng 39*, 1224-1234.

[56] Stroik, D. R., Yuen, S. L., Janicek, K. A., Schaaf, T. M., Li, J., Ceholski, D. K., Hajjar, R. J., Cornea, R. L., and Thomas, D. D. (2018) Targeting protein-protein interactions for therapeutic discovery via FRET-based high-throughput screening in living cells, *Sci Rep 8*, 12560.

[57] Petersen, K. J., Peterson, K. C., Muretta, J. M., Higgins, S. E., Gillispie, G. D., and Thomas, D. D. (2014) Fluorescence lifetime plate reader: resolution and precision meet high-throughput, *Rev Sci Instrum 85*, 113101-113101.

[58] Sy, M., Nonat, A., Hildebrandt, N., and Charbonniere, L. J. (2016) Lanthanide-based luminescence biolabelling, *Chem. Commun. 52*, 5080-5095.

[59] Rajapakse, H. E., Gahlaut, N., Mohandessi, S., Yu, D., Turner, J. R., and Miller, L. W. (2010) Time-resolved luminescence resonance energy transfer imaging of protein-protein interactions in living cells, *Proc Natl Acad Sci U S A 107*, 13582-13587.

[60] Heffern, M. C., Matosziuk, L. M., and Meade, T. J. (2014) Lanthanide probes for bioresponsive imaging, *Chem Rev 114*, 4496-4539.

[61] Selvin, P. R. (2002) Principles and biophysical applications of lanthanide-based probes, *Annu Rev Biophys Biomol Struct 31*, 275-302.

[62] Rajapakse, H. E., Reddy, D. R., Mohandessi, S., Butlin, N. G., and Miller, L. W. (2009) Luminescent terbium protein labels for time-resolved microscopy and screening, *Angew Chem Int Ed Engl 48*, 4990-4992.

[63] Xu, J., Corneillie, T. M., Moore, E. G., Law, G. L., Butlin, N. G., and Raymond, K. N. (2011) Octadentate cages of Tb(III) 2-hydroxyisophthalamides: a new standard for luminescent lanthanide labels, *J Am Chem Soc 133*, 19900-19910.

[64] Miller, L. W., Cai, Y., Sheetz, M. P., and Cornish, V. W. (2005) In vivo protein labeling with trimethoprim conjugates: a flexible chemical tag, *Nat Methods 2*, 255-257.

[65] Welch, C. M., Elliott, H., Danuser, G., and Hahn, K. M. (2011) Imaging the coordination of multiple signalling activities in living cells, *Nat Rev Mol Cell Biol 12*, 749-756.

[66] Fletcher, S., and Hamilton, A. D. (2007) Protein-Protein Interaction Inhibitors: Small Molecules from Screening Techniques, *Current Topics in Medicinal Chemistry 7*, 922-927.

[67] Korn, K., and Krausz, E. (2007) Cell-based high-content screening of small-molecule libraries, *Curr Opin Chem Biol 11*, 503-510.

[68] Scott, D. E., Bayly, A. R., Abell, C., and Skidmore, J. (2016) Small molecules, big targets: drug discovery faces the protein-protein interaction challenge, *Nat Rev Drug Discov 15*, 533-550.

[69] Bünzli, J.-C. G., and Eliseeva, S. V. (2010) Basics of Lanthanide Photophysics, *7*, 1-45.

[70] Gahlaut, N., and Miller, L. W. (2010) Time-resolved microscopy for imaging lanthanide luminescence in living cells, *Cytometry A 77*, 1113-1125.

[71] Rajendran, M., and Miller, L. W. (2015) Evaluating the performance of time-gated live-cell microscopy with lanthanide probes, *Biophys J 109*, 240-248.

[72] Schneider, C. A., Rasband, W. S., and Eliceiri, K. W. (2012) NIH Image to ImageJ: 25 years of image analysis, *Nature Methods 9*, 671-675.

[73] Hildebrandt, N., Wegner, K. D., and Algar, W. R. (2014) Luminescent terbium complexes: Superior Förster resonance energy transfer donors for flexible and sensitive multiplexed biosensing, *Coordination Chemistry Reviews 273-274*, 125-138.

[74] Selvin, P. R. (1996) Lanthanide-based resonance energy transfer, *IEEE Journal of Selected Topics in Quantum Electronics 2*, 1077-1087.

[75] Sivaramakrishnan, S., and Spudich, J. A. (2011) Systematic control of protein interaction using a modular ER/K alpha-helix linker, *Proc Natl Acad Sci U S A 108*, 20467-20472.

[76] Swanson, C. J., and Sivaramakrishnan, S. (2014) Harnessing the unique structural properties of isolated alpha-helices, *J Biol Chem 289*, 25460-25467.

[77] Heyduk, T., and Heyduk, E. (2001) Luminescence energy transfer with lanthanide chelates: interpretation of sensitized acceptor decay amplitudes, *Anal Biochem 289*, 60-67.

[78] Hall, A. (1998) Rho GTPases and the actin cytoskeleton, *Science 279*, 509-514.

[79] Etienne-Manneville, S., and Hall, A. (2002) Rho GTPases in cell biology, *Nature 420*, 629-635.

[80] Raptis, L., Arulanandam, R., Geletu, M., and Turkson, J. (2011) The R(h)oads to Stat3: Stat3 activation by the Rho GTPases, *Exp Cell Res 317*, 1787-1795.

[81] Michaelson, D., Abidi, W., Guardavaccaro, D., Zhou, M., Ahearn, I., Pagano, M., and Philips, M. R. (2008) Rac1 accumulates in the nucleus during the G2 phase of the cell cycle and promotes cell division, *J Cell Biol 181*, 485-496.

[82] Huelsenbeck, S. C., Schorr, A., Roos, W. P., Huelsenbeck, J., Henninger, C., Kaina, B., and Fritz, G. (2012) Rac1 protein signaling is required for DNA damage response stimulated by topoisomerase II poisons, *J Biol Chem 287*, 38590-38599.

[83] Dubash, A. D., Guilluy, C., Srougi, M. C., Boulter, E., Burridge, K., and Garcia-Mata, R. (2011) The small GTPase RhoA localizes to the nucleus and is activated by Net1 and DNA damage signals, *PLoS One 6*, e17380.

[84] Bustelo, X. R., Ojeda, V., Barreira, M., Sauzeau, V., and Castro-Castro, A. (2012) Rac-ing to the plasma membrane: the long and complex work commute of Rac1 during cell signaling, *Small GTPases 3*, 60-66.

[85] Rossman, K. L., Der, C. J., and Sondek, J. (2005) GEF means go: turning on RHO GTPases with guanine nucleotide-exchange factors, *Nat Rev Mol Cell Biol 6*, 167-180.

[86] Moon, S. Y., and Zheng, Y. (2003) Rho GTPase-activating proteins in cell regulation, *Trends Cell Biol 13*, 13-22.

[87] Garcia-Mata, R., Boulter, E., and Burridge, K. (2011) The 'invisible hand': regulation of RHO GTPases by RHOGDIs, *Nat Rev Mol Cell Biol 12*, 493-504.

[88] Fernandez-Zapico, M. E., Gonzalez-Paz, N. C., Weiss, E., Savoy, D. N., Molina, J. R., Fonseca, R., Smyrk, T. C., Chari, S. T., Urrutia, R., and Billadeau, D. D. (2005) Ectopic expression of VAV1 reveals an unexpected role in pancreatic cancer tumorigenesis, *Cancer Cell 7*, 39-49.

[89] Guo, X., Wang, M., Jiang, J., Xie, C., Peng, F., Li, X., Tian, R., and Qin, R. (2013) Balanced Tiam1-rac1 and RhoA drives proliferation and invasion of pancreatic cancer cells, *Mol Cancer Res 11*, 230-239.

[90] Chan, A. Y., Coniglio, S. J., Chuang, Y. Y., Michaelson, D., Knaus, U. G., Philips, M. R., and Symons, M. (2005) Roles of the Rac1 and Rac3 GTPases in human tumor cell invasion, *Oncogene 24*, 7821-7829.

[91] Ferri, N., Corsini, A., Bottino, P., Clerici, F., and Contini, A. (2009) Virtual screening approach for the identification of new Rac1 inhibitors, *J Med Chem 52*, 4087-4090.

[92] Dwivedi, S., Pandey, D., Khandoga, A. L., Brandl, R., and Siess, W. (2010) Rac1-mediated signaling plays a central role in secretion-dependent platelet aggregation in human blood stimulated by atherosclerotic plaque, *J Transl Med 8*, 128.

[93] Arnst, J. L., Hein, A. L., Taylor, M. A., Palermo, N. Y., Contreras, J. I., Sonawane, Y. A., Wahl, A. O., Ouellette, M. M., Natarajan, A., and Yan, Y. (2017) Discovery and characterization of small molecule Rac1 inhibitors, *Oncotarget 8*, 34586-34600.

[94] Gao, Y., Dickerson, J. B., Guo, F., Zheng, J., and Zheng, Y. (2004) Rational design and characterization of a Rac GTPase-specific small molecule inhibitor, *Proc Natl Acad Sci U S A 101*, 7618-7623.

[95] Onesto, C., Shutes, A., Picard, V., Schweighoffer, F., and Der, C. J. (2008) Characterization of EHT 1864, a novel small molecule inhibitor of Rac family small GTPases, *Methods Enzymol 439*, 111-129.

[96] Yan, Y., Hein, A. L., Etekpo, A., Burchett, K. M., Lin, C., Enke, C. A., Batra, S. K., Cowan, K. H., and Ouellette, M. M. (2020) Correction: Inhibition of RAC1 GTPase sensitizes pancreatic cancer cells to gamma-irradiation, *Oncotarget 11*, 304.

[97] Yan, Y., Greer, P. M., Cao, P. T., Kolb, R. H., and Cowan, K. H. (2012) RAC1 GTPase plays an important role in gamma-irradiation induced G2/M checkpoint activation, *Breast Cancer Res 14*, R60.

[98] Reddy, D. R., Pedro Rosa, L. E., and Miller, L. W. (2011) Luminescent trimethoprim-polyaminocarboxylate lanthanide complex conjugates for

selective protein labeling and time-resolved bioassays, *Bioconjug Chem 22*, 1402-1409.

[99] Mohandessi, S., Rajendran, M., Magda, D., and Miller, L. W. (2012) Cell-penetrating peptides as delivery vehicles for a protein-targeted terbium complex, *Chemistry 18*, 10825-10829.

[100] Klomp, J. E., Huyot, V., Ray, A. M., Collins, K. B., Malik, A. B., and Karginov, A. V. (2016) Mimicking transient activation of protein kinases in living cells, *Proc Natl Acad Sci U S A 113*, 14976-14981.

[101] Fritz, G., Brachetti, C., Bahlmann, F., Schmidt, M., and Kaina, B. (2002) Rho GTPases in human breast tumours: expression and mutation analyses and correlation with clinical parameters, *Br J Cancer 87*, 635-644.

[102] Schnelzer, A., Prechtel, D., Knaus, U., Dehne, K., Gerhard, M., Graeff, H., Harbeck, N., Schmitt, M., and Lengyel, E. (2000) Rac1 in human breast cancer: overexpression, mutation analysis, and characterization of a new isoform, Rac1b, *Oncogene 19*, 3013-3020.

[103] Wertheimer, E., Gutierrez-Uzquiza, A., Rosemblit, C., Lopez-Haber, C., Sosa, M. S., and Kazanietz, M. G. (2012) Rac signaling in breast cancer: a tale of GEFs and GAPs, *Cell Signal 24*, 353-362.

APPENDIX

Table 1: Performance measures of FRET biosensors and multi-well assays

Measurements	Definitions	Relevant range
Dynamic range	Dynamic range is the maximum observed difference in either the mean, donor-denominated or acceptor-denominated FRET ratios (*R*). It is calculated with the following formula: $dynamic\ range = \frac{R_{max} - R_{min}}{R_{min}} \times 100\%$	In microscopic imaging, the lower boundary of dynamic range is usually 30%.
Signal-to-noise ratio	Signal-to-noise ratio (*S:N*) represents the precision of imaging data. It is defined as the mean gray value divided by the standard deviation within the region of interest (ROI).	
Z' factor	Z' factor is a standard quality metric for HTS assays. It takes into account the assay signal dynamic range and the data variation in the control measurements. Z' factor is calculated with the following formula: $Z' = 1 - \frac{3(\sigma_p + \sigma_n)}{\mu_p - \mu_n}$ where, σ_p, σ_n and μ_p, μ_n are the standard deviations and means of the positive and negative control wells, respectively.	*Z'* can vary between -∞ and 1, with values > 0.5 considered to be a very good assay, values between 0 and 0.5 considered marginal, and < 0 an unacceptable assay.

Genetically Encodable Fluorescent Biosensors for Tracking Signaling Dynamics in Living Cells

Author: Robert H. Newman, Matthew D. Fosbrink, Jin Zhang

Publication: Chemical Reviews

Publisher: American Chemical Society

Date: May 1, 2011

Fluorescent-Protein-Based Biosensors: Modulation of Energy Transfer as a Design Principle

Author: Robert E. Campbell
Publication: Analytical Chemistry
Publisher: American Chemical Society
Date: Aug 1, 2009

PERMISSION/LICENSE IS GRANTED FOR YOUR ORDER AT NO CHARGE

This type of permission/license, instead of the standard Terms & Conditions, is sent to you because no fee is being charged for your order. Please note the following:

- Permission is granted for your request in both print and electronic formats, and translations.
- If figures and/or tables were requested, they may be adapted or used in part.
- Please print this page for your records and send a copy of it to your publisher/graduate school.
- Appropriate credit for the requested material should be given as follows: "Reprinted (adapted) with permission from (COMPLETE REFERENCE CITATION). Copyright (YEAR) American Chemical Society." Insert appropriate information in place of the capitalized words.
- One-time permission is granted only for the use specified in your request. No additional uses are granted (such as derivative works or other editions). For any other uses, please submit a new request.

If credit is given to another source for the material you requested, permission must be obtained from that source.

BACK CLOSE WINDOW

VITA

HA THI PHAM

Education:

BSc, Chemistry	VNU University of Science	2014

Research Experience:

Graduate Research Assistant at University of Illinois at Chicago	2014 – present
Internship at National University of Singapore	Spring 2014
Internship at University of Illinois at Urbana-Champaign	Summer 2013
Undergraduate Research Assistant at VNU University of Science	2010-2014

Publications:

1. **Pham H. T.**, Miller L. (2019). *High dynamic-range LRET biosensors of Rac1*. Manuscript in preparation.
2. Chen T., **Pham H. T.**, Mohamadi A., Miller L. (2020). *Single-chain lanthanide luminescence biosensors for cell-based imaging and screening of protein-protein interactions.* bioRxiv doi: 10.1101/2020.03.10.985739.
3. Rosenhouse-Dantsker A., **Pham H. T.**, Papadantonakis G. A. *Chem 100 Laboratory Manual.* Chicago: Hayden-McNeil, 2018. Print.
4. Le A. T., Truong H. H., Nguyen P. T., Dao N. T., To T. H., **Pham H. T.**, Soldatenkov A. T., Synthesis and biological activity of (γ-arylpyridino)-dibenzoaza-14-crown-4 ethers, *Mendeleev Communications*, 25(3), 224-225, 2015.
5. Le A. T., Truong H. H., Nguyen P. T., **Pham H. T.**, Kotsuba V. E., Soldatenkov A. T., Khrustalev V. N., Wodajo A. T., Synthesis and Molecular Structure of Dibenzo [4-(α-Thienyl- and α-Pyrrolyl)pyrido]aza-14-crown-4 Ethers, *Macroheterocycles,* 7(4), 386-390, 2014.
6. Girdhar K., Benitez-Jones M., **Pham H. T.**, Nelson M., Gruebele M., Chemla Y., The behavioral space of zebrafish locomotion and its neural network model, *Bulletin of the American Physical Society*, 2014.

Patent:

1. Le A., Soldatenkov T., Nguyen P., To T., Truong H., **Pham H.**, 2013. Synthesis of (γ-arylpyridino)-dibenzoaza-14-crown-4 ether derivatives and their cytotoxicity on four cancer cell lines. *Patent No. VN 19514*.

Awards:

Teaching assistant award	Department of Chemistry, UIC	2016
POSCO scholarship	Posco T.J.Park Fund Foundation	2011-2013